Deuterium Fractionation Survey Toward Protostellar Sources in the Perseus Molecular Cloud: HNC Case

Muneaki Imai, Nami Sakai, Ana López-Sepulcre, Aya E. Higuchi, Yichen Zhang, Yoko Oya, Yoshimasa Watanabe, Takeshi Sakai, Cecilia Ceccarelli, Bertrand Lefloch, et al.

The Astrophysical Journal, 869:51 (26pp), 2018 December 10 https://doi.org/10.3847/1538-4357/aaeb21

Deuterium Fractionation Survey Toward Protostellar Sources in the Perseus Molecular Cloud: HNC Case

Muneaki Imai[1], Nami Sakai[2], Ana López-Sepulcre[1,3], Aya E. Higuchi[2], Yichen Zhang[2], Yoko Oya[1], Yoshimasa Watanabe[1,4,5], Takeshi Sakai[6], Cecilia Ceccarelli[7,8], Bertrand Lefloch[7,8], and Satoshi Yamamoto[1,9]
[1] Department of Physics, The University of Tokyo, 7-3-1, Hongo, Bunkyo-ku, Tokyo 113-0033, Japan
[2] RIKEN Cluster for Pioneering Research, 2-1, Hirosawa, Wako-shi, Saitama 351-0198, Japan
[3] Institut de Radioastronomie Millimétrique (IRAM), 300 rue de la Piscine, F-38406 Saint-Martin-d'Hères, France
[4] Division of Physics, Faculty of Pure and Applied Sciences, University of Tsukuba, Tsukuba, Ibaraki 305-8571, Japan
[5] Center for Integrated Research in Fundamental Science and Engineering (CiRfSE), Faculty of Pure and Applied Sciences, University of Tsukuba, Tsukuba, Ibaraki 305-8571, Japan
[6] Department of Communication Engineering and Informatics, Graduate School of Informatics and Engineering, The University of Electro-Communications, Chofugaoka, Chofu, Tokyo 182-8585, Japan
[7] Universite de Grenoble Alpes, IPAG, F-38000 Grenoble, France
[8] CNRS, IPAG, F-38000 Grenoble, France
[9] Research Center for the Early Universe, The University of Tokyo, 7-3-1, Hongo, Bunkyo-ku, Tokyo 113-0033, Japan
Received 2018 May 18; revised 2018 October 20; accepted 2018 October 22; published 2018 December 11

Abstract

A survey observation of the DNC ($J = 1-0$ and $J = 3-2$) and $HN^{13}C$ ($J = 1-0$ and $J = 3-2$) emission toward 34 Class 0 and I protostellar sources in the Perseus molecular cloud has been conducted with the NRO 45 m and IRAM 30 m telescopes to explore how the deuterium ratio of the neutral species changes after the birth of a protostar. We have detected the $J = 1-0$ and $J = 3-2$ lines of DNC toward 32 sources and the $J = 1-0$ and $J = 3-2$ lines of $HN^{13}C$ toward 31 and 26 sources, respectively. A mean deuterium ratio of HNC, which is defined as $R_D(HNC) = N(DNC)/N(HNC)$, is found to be 0.049–0.056. We compare $R_D(HNC)$ with physical parameters of the sources, and find a negative correlation between $R_D(HNC)$ and the bolometric temperature. This result suggests that $R_D(HNC)$ decreases as a protostar evolves. Compared with the deuterium ratio of the molecular ion N_2H^+, $R_D(HNC)$ seems to decrease slowly with the protostellar evolution.

Key words: ISM: abundances – ISM: molecules – stars: formation – stars: low-mass

1. Introduction

Deuterium fractionation occurs when deuterium atoms are stored in molecules other than HD in a cold and dense environment. Although the elemental D/H ratio is $\sim 10^{-5}$ (Sonneborn et al. 2000; Woodruff et al. 2004; Prodanović et al. 2010), the molecular D/H ratio is often as high as 10^{-3}–10^{-1} (Howe et al. 1994; van Dishoeck et al. 1995; Hirota et al. 2001), which depends on the type of objects (e.g., starless cores, low-mass star-forming regions, or high-mass star-forming regions) and on the molecular species. Given that the degree of deuterium fractionation is sensitive to temperature, the degree of CO depletion onto dust grains, H_2 density, the ortho-to-para ratio of H_2, and chemical evolutionary stages, deuterium fractionation has been extensively employed as a good tracer to study physical conditions and chemical states of interstellar clouds (as described below).

Deuterium fractionation is mainly caused by the following reaction at low temperature:

$$H_3^+ + HD \rightarrow H_2D^+ + H_2 + 230\ K, \quad (1)$$

where para H_2 is implicitly assumed as the product. The formation of H_2D^+ proceeds without a reaction barrier. In contrast, the backward reaction of (1) does not proceed in the cold condition, as far as para H_2 is concerned (Watson 1974; Caselli & Ceccarelli 2012; Albertsson et al. 2013). Note that the backward reaction of (1) can occur and deuterium fractionation does not proceed if the ortho H_2 makes a significant contribution (Pagani et al. 2009). However, the ortho-to-para ratio is close to zero (<0.01) in cold molecular cloud cores (e.g., Dislaire et al. 2012) and, hence, the endothermic nature of the backward reaction leads to an enhanced abundance of H_2D^+ at low temperature. H_2D^+ is further deuterated to make D_2H^+ and D_3^+. These ions donate D^+ to the neutral species to enhance their D/H ratio; for instance, as:

$$H_2D^+ + HNC \rightarrow DNCH^+ + H_2, \quad (2)$$

$$DNCH^+ + e^- \rightarrow DNC + H. \quad (3)$$

Meanwhile, H_3^+ and H_2D^+ are mainly broken up by the reactions with CO as:

$$H_3^+ + CO \rightarrow HCO^+ + H_2, \quad (4)$$

$$H_2D^+ + CO \rightarrow HCO^+ + HD, \quad (5)$$

$$H_2D^+ + CO \rightarrow DCO^+ + H_2. \quad (6)$$

Hence, deuterium fractionation is accelerated once CO is depleted onto dust grains in the dense part of a starless core. Indeed, a number of studies have revealed that the deuterium ratio, R_D, strongly depends on the CO depletion factor (f_D) at low temperatures (Caselli et al. 2002a, 2008; Bacmann et al. 2003; Crapsi et al. 2004, 2005; Emprechtinger et al. 2009; Chen et al. 2011), where the deuterium ratios of HCO^+ ($R_D(HCO^+)$) and N_2H^+ ($R_D(N_2H^+)$) show good correlation with the degree of the CO depletion, f_D. Here, f_D is defined as $f_D = x_{can}(C^{18}O)/x(C^{18}O)$, where $x(C^{18}O)$ and $x_{can}(C^{18}O)$ are the observed and canonical abundances of $C^{18}O$ relative to H_2, respectively. Crapsi et al. (2005) and Emprechtinger et al. (2009) reported a marked increase of $R_D(N_2H^+)$ at f_D larger than 10 in low-mass prestellar cores. Therefore, the deuterium ratio indeed increases with cloud evolution in starless cores.

Hirota et al. (2011b) reported that the DNC/$HN^{13}C$ ratio tends to correlate with the NH_3/CCS ratio, which is often used as an indicator of chemical evolution (e.g., Suzuki et al. 1992; Aikawa et al. 2001; Hirota et al. 2001, 2009).

Deuterium fractionation after the protostar birth has also been studied. For low-mass sources, a negative correlation between dust temperature and $R_D(N_2H^+)$ is claimed by Emprechtinger et al. (2009). This negative correlation is naturally expected for the following two reasons. First, the backward reaction of Reaction (1) becomes possible at a temperature higher than ~25 K. Second, CO can desorb from dust grains above 20 K, which destroys H_3^+ and H_2D^+ through Reactions (4–6). Furthermore, N_2H^+ and N_2D^+ are also destroyed by the reaction with CO. In fact, the decrease of the deuterium ratio is seen at temperatures higher than 20–25 K in their study. For high-mass protostellar sources, Chen et al. (2011), Sakai et al. (2012) and Fontani et al. (2011, 2014) confirmed this trend by observing the deuterium ratios of HNC and N_2H^+ in infrared dark clouds. The negative correlation of the deuterium ratios with the gas kinetic temperature is also consistent with the above picture for the low-mass sources. Sakai et al. (2012) and Fontani et al. (2014) conducted chemical model simulations of deuterium fractionation and revealed the decrease of the ratio after the temperature rise due to the protostar birth. This behavior is more prominent in N_2H^+ than in HNC.

In a statistical approach, Friesen et al. (2013) performed a survey observation of the deuterium ratio of N_2H^+ toward 64 low-mass starless and protostellar sources in the Perseus molecular cloud complex. The Perseus molecular cloud is a nearby low-mass star-forming region at a distance of 235 pc (Hirota et al. 2008, 2011a), and harbors a large number of Class 0 and I protostars. It is characterized by a low CO depletion degree, where most of the sources show f_D less than 10. Friesen et al. (2013) reported that $R_D(N_2H^+)$ increases as the H_2 column density increases. They also claimed that there is a negative correlation between $R_D(N_2H^+)$ and the bolometric temperature of the protostar.

In this study, we focus on the deuterium fractionation of the neutral species HNC in low-mass protostellar sources in the Perseus molecular cloud because the decrease of the deuterium ratio for neutral species is expected to be different from that for molecular ions like N_2H^+, according to the chemical model calculation (Sakai et al. 2012). This is due to the different reactivities of neutral species and molecular ions. For instance, the N_2H^+ can be easily destructed by a reaction with CO as:

$$N_2H^+ + CO \rightarrow HCO^+ + N_2. \quad (7)$$

Then, the destruction timescale for N_2H^+ is roughly given as $\tau \sim 1/k_1 n(CO) \sim 4$ yr, where k_1 is the rate coefficient for Reaction (7). Here, $n(X)$ denotes the number density of molecule X. Meanwhile, the main destruction pathway of HNC is a reaction with HCO^+ as:

$$HNC + HCO^+ \rightarrow HNCH^+ + CO. \quad (8)$$

Then, the destruction timescale for HNC is estimated as $\tau \sim 1/k_2 n(HCO^+) \sim 3 \times 10^4$ yr, where k_2 is the rate coefficient for Reaction (8). The different behavior of the neutral species in the deuterium fractionation, if confirmed, would be an important clue to understanding a variation in deuterium fractionation along with the protostellar evolution. With this in mind, we measured the deuterium ratio of HNC toward 34 Class 0 and I protostellar sources.

2. Observation

2.1. Target Sources and Observed Lines

We selected the target sources in the Perseus molecular cloud from the list by Hatchell et al. (2007) under the following criteria: (1) the protostellar sources are in the Class 0 or I stage; (2) the bolometric luminosity is higher than 1.0 $L_\odot$ (except for B1-5; 0.7 $L_\odot$ in the list by Hatchell et al. 2007); and (3) the envelope mass is higher than 1.0 $M_\odot$ to ensure association of a substantial amount of molecular gas. In total, 34 low-mass protostellar sources are selected (Table 1). NGC 1333 IRAS 4A and SVS 13A are excluded, although they satisfy the above criterion. Aside from these exceptions, our sample list covers all sources that fulfill the above criteria, and is the same as that employed by Higuchi et al. (2018) (the source ID is also common). Among our sample, 18 sources are in Friesen et al.'s (2013) source catalog. The values of the bolometric temperature and the bolometric luminosity are taken from Tobin et al. (2016) instead of Hatchell et al. (2007) in our analysis because they take into account the multiplicity of the sources. Tobin et al.'s (2016) source catalog has 26 sources. Our sample is unbiased under the above three conditions. It should be stressed that it is unbiased from a chemical point of view. The sources are distributed over the Perseus molecular cloud and are in various physical environments, such as clusters and isolated cores. To assess the deuterium ratio of HNC, we observed the lines of DNC and $HN^{13}C$ because the lines of the normal species HNC are often optically thick (e.g., Hirota et al. 1998). The $J = 1-0$ and $J = 3-2$ lines of DNC and $HN^{13}C$ (Table 2) were observed with the NRO 45 m and IRAM 30 m telescopes, as described below.

2.2. Observation with the NRO 45 m Telescope

We observed the $J = 1-0$ lines of DNC (76.3056995 GHz) and $HN^{13}C$ (87.0908252 GHz) with the NRO 45 m telescope on 2015 March 22–28. The two lines were observed simultaneously. The frontend and the backend were the two sideband receiver, T70, and the SAM 45 spectrometer, respectively. The beam size was 21.″3 for DNC ($J = 1-0$) and 20.″4 for $HN^{13}C$ ($J = 1-0$). These beam sizes almost correspond to 4000 au at the distance to the Perseus molecular cloud and are roughly comparable to a typical size of a protostellar envelope (a few 1000 au). Bandwidth and channel spacing of the spectrometer are 4 GHz and 122.1 kHz (0.48 km s^{-1}), respectively. The line intensities were calibrated by the chopper wheel method. The accuracy of the calibration are estimated to be better than 20%. The observation was conducted by the position switching mode, where the off-position was taken to be the line-free position. The offset of the off-position relative to the target source position is (δR.A., δdecl.) = (0″, 780″) for the sources in the L1455 region, (−850″, 0″) for the sources in the B1 region, (−600″, 0″) for the sources in the IC 348, Barnard 5, and L1448 regions, and (−1200″, 0″) for the sources in the NGC 1333 region. The integrated intensities of the $J = 1-0$ line of $C^{18}O$ at these off-positions are confirmed to be weaker than 1 K km s^{-1} in the map reported by Hatchell et al. (2005). The telescope pointing was checked by observing nearby SiO maser sources every one or two hours, and was maintained to be better than 7″. The main-beam temperature (T_{MB}) is derived with a correction of the telescope efficiency, which is obtained by comparing the integrated intensities of the CCH ($N = 1-0$, $J = 3/2-1/2$,

Table 1
Observed Sources

Source[a]	R.A.(J2000)	Decl.(J2000)	Class[b]	T_{bol}[c] (K)	L_{bol}[b] ($L_\odot$)	Other Names
NGC 1333-1	$3^h29^m12\overset{s}{.}01$	31°13′08.″2	0	28 ± 1	4.0 ± 0.3	IRAS 4B
NGC 1333-2	$3^h28^m55\overset{s}{.}57$	31°14′37.″1	0	69 ± 1	19.0 ± 0.4	IRAS 2A
NGC 1333-3	$3^h29^m01\overset{s}{.}66$	31°20′28.″5	(I)	–	–	SK24
NGC 1333-4	$3^h29^m10\overset{s}{.}72$	31°18′20.″5	0	45 ± 12	6.9 ± 1.9	SK 20
NGC 1333-5	$3^h29^m13\overset{s}{.}62$	31°13′57.″9	0	31 ± 2	0.70 ± 0.08	IRAS 4C; SK 5
NGC 1333-6	$3^h28^m37\overset{s}{.}11$	31°13′28.″3	I	103 ± 26	9.1 ± 0.3	IRAS 1; SK 6
NGC 1333-7	$3^h29^m06\overset{s}{.}50$	31°15′38.″6	(I)	–	–	HH7-11 MMS 1; SK 15
NGC 1333-8	$3^h29^m04\overset{s}{.}90$	31°14′46.″6	0	36 ± 4	0.4 ± 0.1	HH7-11 MMS 6; SK14
NGC 1333-9	$3^h29^m10\overset{s}{.}70$	31°21′45.″3	(I)	–	–	SK 28
NGC 1333-10	$3^h29^m07\overset{s}{.}70$	31°21′56.″8	I	128 ± 23	23.2 ± 3	SK 29
NGC 1333-11	$3^h29^m07\overset{s}{.}10$	31°17′23.″7	(0)	–	–	SK 18
NGC 1333-12	$3^h29^m18\overset{s}{.}25$	31°23′19.″9	(I)	–	–	SK 32
NGC 1333-13	$3^h29^m19\overset{s}{.}70$	31°23′56.″0	(I)	–	–	
NGC 1333-14	$3^h28^m56\overset{s}{.}20$	31°19′12.″5	(0)	–	–	
NGC 1333-15	$3^h29^m15\overset{s}{.}30$	31°20′31.″2	(0)	–	–	SK 22
L1448-1	$3^h25^m35\overset{s}{.}66$	30°45′14.″8	0	22 ± 1	1.4 ± 0.1	L1448NW
L1448-2	$3^h25^m36\overset{s}{.}33$	30°45′14.″8	0	57 ± 3	8.3 ± 0.8	L1448NB
L1448-3	$3^h25^m38\overset{s}{.}87$	30°44′05.″3	0	47 ± 7	8.4 ± 1.5	L1448C
L1448-4	$3^h25^m22\overset{s}{.}38$	30°45′13.″3	0	43 ± 2	3.6 ± 0.5	L1448-IRS2
L1448-5	$3^h25^m25\overset{s}{.}90$	30°45′02.″7	0	15 ± −99	0.05 ± 0.05	L1448-IRS2E
IC 348-1	$3^h43^m56\overset{s}{.}80$	32°00′50.″3	0	27 ± 1	1.8 ± 0.1	HH211-MMS
IC 348-2	$3^h43^m57\overset{s}{.}05$	32°03′05.″0	0	30 ± 2	1.5 ± 0.1	IC 348-MMS
IC 348-3	$3^h44^m43\overset{s}{.}32$	32°01′31.″6	I	309 ± 64	1.8 ± 0.8	
IC 348-4	$3^h43^m50\overset{s}{.}99$	32°03′24.″7	0	39 ± 2	0.40 ± 0.04	
B5	$3^h47^m41\overset{s}{.}61$	32°51′43.″9	I	287 ± 8	4.7 ± 0.9	Barnard5 IRS1
B1-1	$3^h33^m17\overset{s}{.}87$	31°09′32.″3	0	48 ± 1	3.7 ± 0.4	B1-c
B1-2	$3^h33^m16\overset{s}{.}49$	31°06′52.″3	0	30 ± 2	0.6 ± 0.05	B1-d
B1-3	$3^h33^m16\overset{s}{.}67$	31°07′55.″1	I	132 ± 25	1.5 ± 1	B1-a
B1-4	$3^h32^m18\overset{s}{.}03$	30°49′46.″9	0	27 ± 1	0.90 ± 0.07	
B1-5	$3^h31^m20\overset{s}{.}94$	30°45′30.″3	0	32 ± 2	1.3 ± 0.1[d]	
L1455-1	$3^h26^m37\overset{s}{.}46$	30°15′28.″2	0	61 ± 1	1.2 ± 0.02	
L1455-2	$3^h27^m39\overset{s}{.}11$	30°13′02.″8	0	59 ± 11	4.2 ± 0.1	L1455 IRS 1
L1455-3	$3^h27^m43\overset{s}{.}25$	30°12′28.″9	0	65 ± 3	1.4 ± 0.2	L1455 IRS 4
L1455-4	$3^h27^m47\overset{s}{.}69$	30°12′04.″4	I	740 ± −99	2.5 ± 0.1	L1455 IRS 2
			Calibration Source			
L1527	$4^h39^m53\overset{s}{.}90$	26°03′09.″6	0	44[e]	2.0[e]	

Notes.
[a] The source ID is the same as that in Higuchi et al. (2018). NGC 1333-16 (IRAS 4A) and NGC 1333-17 (SVS 13A) are excluded from our sample.
[b] Parentheses indicate the Class 0/I classification taken from Hatchell et al. (2007). For the other sources, the classification is taken from Tobin et al. (2016). We define the sources with $T_{bol} < 70$ as Class 0 and those with $T_{bol} \geqslant 70$ as Class I (Evans et al. 2009).
[c] T_{bol} and L_{bol} are taken from Tobin et al. (2016). The sources that are not listed in Tobin et al. (2016) are indicated by –.
[d] Taken from Tobin et al. (2016). Note that L_{bol} is 0.7 $L_\odot$ in the list of Hatchell et al. (2007) (Section 2.1).
[e] T_{bol} and L_{bol} for L1527 are taken from Kristensen et al. (2012).

Table 2
Observed Lines

Species	Transition	Rest Frequency (GHz)	E_u (cm^{-1})	$S\mu^2$ ($Debye^2$)	Telescope	f_{bw}[a] (GHz)	f_{res}[a] (kHz)	θ_{FWHM}[b] (″)	η_{MB}[c]	T_{sys} (K)	Observation Period
DNC	$J = 1-0$	76.3056995	2.55	9.30	NRO 45 m	2	122.1	21.7	0.48	190	2015 Mar 22–28
$HN^{13}C$	$J = 1-0$	87.0908252	2.91	9.30	NRO 45 m	2	122.1	20.7	0.45	150	2015 Mar 22–28
DNC	$J = 3-2$	228.9104810	15.27	27.91	IRAM 30 m	16	194.9	10.7	0.46	200	2015 Dec 23–29
$HN^{13}C$	$J = 3-2$	261.2635132	17.43	27.91	IRAM 30 m	16	194.9	9.0	0.41	240	2015 Mar 22–29

Notes.
[a] f_{bw} and f_{res} denote the bandwidth and channel spacing of the spectrometer, respectively.
[b] θ_{FWHM} denotes the full width of the half maximum of the beam.
[c] η_{MB} for IRAM 30 m telescope is calculated by $\eta_{MB} = B_{eff}/F_{eff}$.

$F = 2-1$) and DNC ($J = 1-0$) lines observed daily toward L1527 with the standard values measured by Yoshida et al. (2018) (5.97 K km s^{-1}) and Y. Nishimura et al. (2018, private communication) (2.02 K km s^{-1}), respectively. The observed data were reduced with the software package NEWSTAR developed by NRO.

2.3. Observation with the IRAM 30 m Telescope

We observed the $J = 3-2$ lines of DNC (228.9104810 GHz) and HN^{13}C (261.2635132 GHz) with the IRAM 30 m telescope on 2015 December 23–29 for DNC and 2015 March 22–29 for HN^{13}C. These lines were observed separately. The frontend and the backend of the IRAM 30 m telescope were the EMIR heterodyne receiver and FTS200, respectively. The beam size was 10.″7 for DNC and 9.″0 for HN^{13}C. These beam sizes are smaller than those in the observations with the NRO 45 m telescope by a factor of 2. Bandwidth and channel spacing of the spectrometer are 16 GHz and 194.9 kHz (0.25 km s^{-1}), respectively As in the NRO 45 m observation, the observation was conducted by the position switching mode. The off-positions are the same as those for NRO 45 m observation. The telescope pointing was checked by observing nearby continuum sources every one or two hours, and was maintained to be better than 3″. The line intensities were calibrated by the two temperature loads, where the calibration accuracy is ∼20%. The main-beam temperature is derived by $T_{\rm MB} = T_{\rm a}^{*} \times F_{\rm eff}/B_{\rm eff}$, where $B_{\rm eff}$ is the main-beam efficiency, $F_{\rm eff}$ is the forward efficiency, and $T_{\rm a}^{*}$ is the antenna temperature. The $B_{\rm eff}$ and $F_{\rm eff}$ values are 0.59 and 0.92 for DNC ($J = 3-2$), respectively, and 0.53 and 0.92 for HN^{13}C ($J = 3-2$), respectively. The data were reduced with the software CLASS of the GILDAS package developed by IRAM.

3. Results

3.1. Observation Results and Line Parameters

The $J = 1-0$ and $J = 3-2$ lines of DNC were detected with a confidence level of 3σ or higher in 32 sources. They were not detected in the two sources, NGC 1333-9 and NGC 1333-10. The $J = 1-0$ line of HN^{13}C was detected with the above criterion in 31 sources, while it was not detected in the three sources, NGC 1333-9, NGC 1333-10, and NGC 1333-15. The $J = 3-2$ line of HN^{13}C was detected above the 3σ noise level in 26 sources. Generally speaking, the intensities of the DNC lines are stronger than those of the HN^{13}C lines. All of the observed spectra are shown in Appendix A.

The line parameters were obtained by Gaussian fitting, as summarized in Tables 3 and 4. The lines of DNC and HN^{13}C are split into hyperfine components mainly due to the nuclear spins of the N and D nuclei (van der Tak et al. 2009). This splitting is particularly significant for the $J = 1-0$ lines, which broadens the observed line widths (the velocity shifts and relative intensities for the hyperfine components are shown in Appendix B). Hence, we tried to fit the multiple Gaussian function to the observed spectral profiles of the $J = 1-0$ lines by considering the optical depths and the excitation temperature as free parameters. However, the fitting was unsuccessful for most of the observed sources because of heavy blending of the hyperfine components. Hence, each spectral line profile was fitted using a single Gaussian function without considering the hyperfine splitting. In some sources, the line width corresponds to only 3–4 spectral channels, and the line shape is not clearly resolved. Hence, the line shape can be affected by the hyperfine structure in such sources. The uncertainty of these effects is not included in the fitting parameters given in Tables 3 and 4. Alternatively, we confirmed that the integrated intensity calculated from the Gaussian fitting parameters agrees with the integrated intensity calculated directly, within the error limits (Tables 3 and 4). In this study, we derive the column density with the large velocity gradient (LVG) analysis using the fitting parameters in Section 3.3. The uncertainty due to the non-Gaussian line shape should not significantly affect the uncertainty of the column density because the column density in the LVG analysis is mostly determined by the integrated intensity.

3.2. DNC/HN^{13}C Intensity Ratios

Since the frequency of the $J = 3-2$ line is about three times the frequency of the $J = 1-0$ line, the critical density of the $J = 3-2$ line is typically higher by a factor of about 30 than that of the $J = 1-0$ line. Furthermore, the beam size for the $J = 1-0$ line is twice as large as that for the $J = 3-2$ line. The source structure (i.e., size and density structure) is unknown for most of the observed sources, so that the simultaneous analysis using both the $J = 1-0$ and $J = 3-2$ lines might introduce systematic errors due to assumptions made about the source structure. Therefore, in this paper we analyze the $J = 1-0$ and $J = 3-2$ lines separately to derive information of the beam-averaged deuterium ratios and we then compare their results.

First, we prepare the correlation diagram of the integrated intensities of DNC and HN^{13}C each for the $J = 1-0$ and $J = 3-2$ lines (Figure 1). The integrated intensities of DNC linearly correlate with those of HN^{13}C for both of the $J = 1-0$ and $J = 3-2$ lines, where the correlation coefficient is 0.93 and 0.68, respectively. Nevertheless, the DNC/HN^{13}C integrated intensity ratio, $R_{\rm W}$, is slightly different from source to source. The ratio has a range of a factor of 3–5. We then compare the DNC/HN^{13}C integrated intensity ratio for the $J = 3-2$ line with that for the $J = 1-0$ line, as shown in Figure 2. The intensity ratios for both the transitions correlate well with each other. Moreover, the intensity ratio for the $J = 3-2$ line tends to be higher than that for the $J = 1-0$ line by a factor of 2.

Under the local thermal equilibrium (LTE) condition, the slightly higher upper state energy of HN^{13}C than that of DNC can cause the higher integrated intensity ratio of DNC/HN^{13}C, especially in the cold condition. However, the difference of a factor of 2 cannot be fully explained by this effect, as described in Appendix C. This might suggest that the emitting region of the $J = 3-2$ lines would have a higher deuterium ratio than that of the $J = 1-0$ lines. Alternatively, the excitation temperatures of the two lines are likely to be different because the critical density of the $J = 3-2$ line is much higher than that of the $J = 1-0$ line. Hence, we conduct the non-LTE analysis using the LVG model.

3.3. LVG Analysis

To derive the column densities of DNC and HN^{13}C, we employ the non-LTE molecular radiative transfer code RADEX (van der Tak et al. 2007), assuming the gas kinetic temperature and H_2 density. The collisional rates for HNC are also employed for DNC and HN^{13}C. The $J = 3-2$ lines should better trace the central region than the $J = 1-0$ lines, considering the smaller beam size and the higher critical densities (∼5 × 10^{6} cm^{-3}). Hence, we assume the H_2 density

Table 3
Fitting Results for DNC

Source	DNC ($J = 1-0$)					DNC ($J = 3-2$)				
	W[a] (K km s^{-1})	T_{peak}[b] (K)	V_{LSR}[b] (km s^{-1})	Δv[b] (km s^{-1})	σ_{rms} (K)	W[a] (K km s^{-1})	T_{peak}[b] (K)	V_{LSR}[b] (km s^{-1})	Δv[b] (km s^{-1})	σ_{rms} (K)
NGC 1333-1	2.34(3)	1.40(5)	6.99(3)	1.59(7)	0.021	1.35(2)	1.26(8)	6.83(3)	1.00(8)	0.027
NGC 1333-2	1.78(5)	1.26(4)	7.47(2)	1.34(5)	0.040	1.26(2)	1.48(5)	7.486(13)	0.78(3)	0.029
NGC 1333-3	3.72(5)	3.10(7)	7.964(12)	1.12(3)	0.041	2.08(2)	2.69(7)	8.196(9)	0.72(2)	0.033
NGC 1333-4	2.59(9)	2.18(12)	8.57(3)	1.10(7)	0.078	0.87(2)	1.43(4)	8.641(7)	0.567(17)	0.037
NGC 1333-5	3.27(4)	2.40(4)	7.778(11)	1.26(3)	0.036	0.641(14)	0.599(13)	7.646(11)	1.04(3)	0.020
NGC 1333-6	0.92(4)	0.72(4)	7.22(3)	1.21(7)	0.030	0.360(17)	0.46(3)	7.26(2)	0.76(5)	0.028
NGC 1333-7	3.75(3)	2.56(7)	7.952(18)	1.35(4)	0.029	0.84(2)	1.08(6)	8.092(18)	0.72(4)	0.030
NGC 1333-8	3.05(5)	1.91(13)	6.91(5)	1.46(12)	0.036	0.78(2)	1.06(6)	6.71(2)	0.67(5)	0.034
NGC 1333-9[c]	*	*	*	*	0.044	*	*	*	*	0.016
NGC 1333-10[c]	*	*	*	*	0.044	*	*	*	*	0.017
NGC 1333-11	3.40(7)	2.85(13)	8.49(2)	1.11(6)	0.067	0.592(13)	0.82(5)	8.540(18)	0.65(4)	0.021
NGC 1333-12	0.38(8)	0.53(9)	7.3(2)	1.1(6)	0.071	0.102(9)	0.22(3)	7.51(3)	0.43(7)	0.021
NGC 1333-13	0.23(6)	0.26(6)	7.52(9)	0.8(3)	0.067	0.041(7)	0.084(10)	7.62(3)	0.46(6)	0.018
NGC 1333-14	2.20(8)	2.04(12)	7.75(3)	0.99(7)	0.072	0.460(10)	0.78(2)	7.863(8)	0.551(19)	0.018
NGC 1333-15	0.19(6)	0.21(3)	7.2(4)	1.4(7)	0.069	0.333(9)	0.574(18)	8.346(8)	0.538(19)	0.017
L1448-1	7.42(5)	5.18(9)	4.356(11)	1.35(3)	0.037	1.95(3)	1.58(6)	4.20(2)	1.17(5)	0.029
L1448-2	6.75(6)	4.79(12)	4.504(16)	1.32(4)	0.049	1.96(2)	1.63(9)	4.42(3)	1.13(7)	0.028
L1448-3	4.52(5)	2.90(9)	5.25(2)	1.47(5)	0.035	1.327(19)	1.41(3)	4.949(8)	0.889(19)	0.025
L1448-4	3.52(7)	3.19(13)	4.04(2)	1.06(5)	0.057	0.583(15)	0.90(2)	4.070(8)	0.63(2)	0.028
L1448-5	4.99(6)	4.1(2)	4.05(3)	1.13(6)	0.054	0.577(17)	0.82(3)	4.019(14)	0.66(3)	0.028
IC 348-1	4.95(7)	4.03(13)	9.033(19)	1.13(4)	0.066	1.21(2)	1.62(3)	9.134(6)	0.704(15)	0.035
IC 348-2	1.39(10)	1.44(11)	8.68(4)	0.95(8)	0.061	0.64(2)	1.04(4)	8.756(10)	0.56(2)	0.033
IC 348-3	0.44(8)	0.22(5)	10.31(19)	1.6(4)	0.053	0.105(13)	0.074(12)	10.37(10)	1.3(2)	0.017
IC 348-4	3.08(8)	2.95(13)	8.50(2)	0.98(5)	0.067	0.686(16)	1.36(4)	8.486(7)	0.478(14)	0.036
B5	2.77(5)	2.31(8)	10.25(2)	1.13(5)	0.045	0.312(17)	0.46(5)	10.17(3)	0.66(8)	0.030
B1-1	6.05(7)	4.4(2)	6.14(3)	1.27(6)	0.064	1.71(2)	1.77(13)	6.19(3)	0.92(8)	0.032
B1-2	5.36(8)	3.98(19)	6.36(3)	1.28(7)	0.072	0.765(16)	0.98(7)	6.45(3)	0.76(7)	0.029
B1-3	2.73(7)	2.04(9)	6.26(3)	1.24(6)	0.057	0.208(15)	0.26(3)	6.18(4)	0.75(8)	0.029
B1-4	4.42(6)	3.80(10)	6.854(14)	1.10(3)	0.055	1.078(19)	1.26(3)	6.852(8)	0.82(2)	0.030
B1-5	3.95(7)	3.40(14)	6.90(2)	1.10(5)	0.058	1.184(17)	1.70(8)	6.893(16)	0.66(4)	0.028
L1455-1	1.30(4)	1.12(7)	15.10(3)[d]	1.09(8)	0.031	0.333(12)	0.55(3)	5.226(14)	0.58(3)	0.024
L1455-2	1.48(4)	1.18(8)	14.86(4)[d]	1.20(10)	0.039	0.521(16)	0.64(3)	4.926(18)	0.80(4)	0.028
L1455-3	1.68(5)	1.42(11)	14.88(4)[d]	1.09(10)	0.046	0.376(14)	0.67(3)	4.818(12)	0.54(3)	0.028
L1455-4	0.96(4)	0.78(4)	14.92(3)[d]	1.13(7)	0.038	0.056(8)	0.12(2)	4.95(3)	0.45(10)	0.019
					Calibration Source					
L1527	1.95(5)	1.88(9)	5.80(2)	0.96(6)	0.043	0.37(2)	0.474(15)	5.925(12)	0.73(3)	0.029

Notes.
[a] The error of the integrated intensity (W) is derived by using the following formula: $\Delta W = \sigma_{rms} \times \sqrt{v_w \Delta v_{res}}$, where v_w represents the width of the integrated velocity range, σ_{rms} the rms noise per spectral channel, and Δv_{res} the spectral channel width in velocity.
[b] The peak intensity (T_{peak}), the systemic velocity (V_{LSR}), and the velocity width (Δv) are derived by a Gaussian fit.
[c] The $J = 1-0$ and/or $J = 3-2$ lines of DNC were not detected in this source. Only the rms noise is given. The other columns are marked with $*$.
[d] V_{LSR} is as large as 10 km s^{-1} in L1455 region, owing to a technical trouble in the NRO 45 m observation. All of the molecular lines are shifted about 10 km s^{-1} in L1455 region. This deviation is not confirmed in the IRAM 30 m observation.

of 1×10^5, 3×10^5, and 1×10^7 cm^{-3} for the $J = 3-2$ lines and 3×10^4, 1×10^5, and 3×10^5 cm^{-3} for the $J = 1-0$ lines. Considering the high critical density of the $J = 3-2$ line, we set the highest H_2 density to be 1×10^7 cm^{-3} to investigate the condition close to the thermal equilibrium condition. The kinetic temperature is assumed to be 20 K, the temperature dependence will be mentioned later. The beam-averaged column densities are derived for each line of DNC and HN^{13}C. An uncertainty of the column density derived for each assumed H_2 density is evaluated to satisfy the following inequality:

$$\left(\frac{I^{(n+1)-n} - I_{cal}^{(n+1)-n}}{\sigma_{I^{(n+1)-n}}} \right)^2 < 1, \quad (9)$$

where $I^{(n+1)-n}$ and $I_{cal}^{(n+1)-n}$ are the observed and calculated intensities of the $J = (n+1)-n$ line, respectively, and $\sigma_{I^{(n+1)-n}}$ is the error of the observed intensities of the $J = (n+1)-n$ line. The fitting and calibration errors are included in this error. We estimate the deuterium ratio (R_D(HNC) = N(DNC)/N(HNC)) using the column densities of DNC and HN^{13}C obtained for the same H_2 density. This is based on the assumption that the DNC and HN^{13}C lines come from the same region. The R_D(HNC) is evaluated each for the $J = 1-0$ and $J = 3-2$ data. In the conversion of the column density ratio of N(DNC)/N(HN^{13}C) into R_D(HNC), we assume the ^{12}C/^{13}C isotopic ratio. Lucas & Liszt (1998) and Milam et al. (2005) reported its ratio to be 60–70. In this paper, we employ the ratio of 60. The uncertainty of

Table 4
Fitting Results for $HN^{13}C$

Source	$HN^{13}C$ ($J = 1-0$)					$HN^{13}C$ ($J = 3-2$)				
	W[a] (K km s^{-1})	T_{peak}[b] (K)	V_{LSR}[b] (km s^{-1})	Δv[b] (km s^{-1})	σ_{rms} (K)	W[a] (K km s^{-1})	T_{peak}[b] (K)	V_{LSR}[b] (km s^{-1})	Δv[b] (km s^{-1})	σ_{rms} (K)
NGC 1333-1	1.10(4)	0.58(3)	7.07(5)	1.79(11)	0.026	0.30(3)	0.139(13)	6.75(8)	1.8(2)	0.028
NGC 1333-2	1.39(3)	0.986(14)	7.555(9)	1.31(2)	0.027	0.85(4)	0.61(3)	7.37(3)	0.99(6)	0.037
NGC 1333-3	1.07(3)	0.98(4)	7.873(19)	1.01(4)	0.027	0.467(14)	0.61(2)	8.086(14)	0.70(3)	0.021
NGC 1333-4	0.89(5)	0.93(3)	8.654(14)	0.90(3)	0.048	0.189(18)	0.328(15)	8.514(12)	0.51(3)	0.031
NGC 1333-5	1.07(3)	0.98(4)	7.873(19)	1.01(4)	0.027	0.12(2)	0.129(19)	7.68(7)	0.92(16)	0.030
NGC 1333-6	0.68(4)	0.58(2)	7.206(19)	1.09(4)	0.035	0.19(2)	0.19(2)	7.20(6)	0.96(14)	0.031
NGC 1333-7	1.71(3)	1.32(4)	8.081(19)	1.20(4)	0.028	0.23(2)	0.202(11)	8.01(3)	1.02(6)	0.025
NGC 1333-8	1.41(4)	0.83(5)	7.07(5)	1.59(12)	0.032	0.146(18)	0.153(14)	6.58(4)	0.93(10)	0.026
NGC 1333-9[c]	*	*	*	*	0.034	*	*	*	*	0.024
NGC 1333-10[c]	*	*	*	*	0.034	*	*	*	*	0.024
NGC 1333-11	0.81(4)	0.82(5)	8.55(3)	0.91(6)	0.041	0.067(13)	0.09(2)	8.45(7)	0.63(17)	0.026
NGC 1333-12[c]	0.24(3)	0.23(3)	7.47(8)	1.08(19)	0.033	*	*	*	*	0.026
NGC 1333-13[c]	0.30(4)	0.29(4)	7.58(5)	0.87(12)	0.036	*	*	*	*	0.024
NGC 1333-14	0.90(5)	0.84(5)	7.82(3)	0.98(6)	0.044	0.082(17)	0.097(12)	7.69(5)	0.83(12)	0.029
NGC 1333-15[c]	*	*	*	*	0.038	*	*	*	*	0.024
L1448-1	2.81(4)	2.14(2)	4.474(6)	1.232(14)	0.038	0.40(2)	0.290(19)	4.11(4)	1.34(10)	0.027
L1448-2	2.96(3)	2.19(4)	4.647(13)	1.27(3)	0.029	0.41(2)	0.284(17)	4.55(4)	1.37(10)	0.028
L1448-3	1.95(4)	1.36(5)	5.22(3)	1.36(6)	0.034	0.38(2)	0.42(3)	4.94(3)	0.86(8)	0.036
L1448-4	1.61(5)	1.61(7)	4.081(18)	0.90(4)	0.042	0.277(18)	0.406(17)	4.035(13)	0.62(3)	0.029
L1448-5	1.88(4)	1.92(11)	4.14(3)	0.91(6)	0.037	0.089(15)	0.23(4)	4.01(4)	0.41(8)	0.038
IC 348-1	1.50(5)	1.49(8)	9.04(2)	0.91(5)	0.050	0.29(2)	0.38(3)	8.95(3)	0.70(7)	0.036
IC 348-2	0.80(7)	0.53(5)	8.70(6)	1.16(14)	0.046	0.17(2)	0.24(3)	8.67(3)	0.59(8)	0.029
IC 348-3[c]	0.26(4)	0.14(2)	9.97(14)	1.7(3)	0.040	*	*	*	*	0.028
IC 348-4	1.67(5)	1.61(6)	8.547(16)	0.94(4)	0.044	0.211(15)	0.31(2)	8.42(2)	0.58(5)	0.024
B5	1.01(4)	1.068(13)	10.274(5)	0.889(13)	0.043	0.107(18)	0.087(15)	10.10(10)	1.2(2)	0.025
B1-1	2.28(4)	2.01(12)	6.26(3)	1.09(7)	0.041	0.32(2)	0.36(3)	6.19(3)	0.78(7)	0.036
B1-2	2.32(5)	2.15(7)	6.402(16)	1.02(4)	0.047	0.137(16)	0.21(2)	6.34(4)	0.67(9)	0.032
B1-3[c]	1.38(7)	1.09(6)	6.33(3)	1.15(7)	0.056	*	*	*	*	0.028
B1-4	1.74(5)	1.78(8)	6.88(2)	0.90(5)	0.053	0.207(19)	0.21(2)	6.92(6)	0.96(13)	0.032
B1-5	1.43(4)	1.59(9)	6.86(2)	0.82(5)	0.040	0.178(13)	0.316(17)	6.823(14)	0.54(3)	0.026
L1455-1	0.69(3)	0.65(3)	15.13(2)[d]	0.99(6)	0.030	0.084(13)	0.127(19)	5.17(5)	0.64(11)	0.025
L1455-2	0.91(3)	0.81(2)	14.875(13)[d]	1.07(3)	0.031	0.153(16)	0.138(19)	4.88(8)	1.11(18)	0.028
L1455-3	1.02(4)	0.92(5)	15.01(3)[d]	1.02(7)	0.038	0.120(13)	0.160(15)	4.82(3)	0.71(8)	0.027
L1455-4[c]	0.72(5)	0.70(3)	15.03(2)[d]	0.97(5)	0.047	*	*	*	*	0.028
Calibration Source										
L1527[e]	0.960(18)	1.03(2)	5.878(10)	0.89(2)	0.022	–	–	–	–	–

Notes.
[a] The error of the integrated intensity (W) is derived by using the following formula: $\Delta W = \sigma_{rms} \times \sqrt{v_w \Delta v_{res}}$, where v_w represents the width of the integrated velocity range, σ_{rms} the rms noise per spectral channel, and Δv_{res} the spectral channel width in velocity.
[b] The peak intensity (T_{peak}), the systemic velocity (V_{LSR}), and the velocity width (Δv) are derived by a Gaussian fit.
[c] The $J = 1-0$ and/or $J = 3-2$ lines of $HN^{13}C$ were not detected in this source. Only the rms noise is given. The other columns are marked with *.
[d] V_{LSR} is as large as 10 km s^{-1} in L1455 region, owing to a technical trouble in the NRO 45 m observation. All of the molecular lines are shifted about 10 km s^{-1} in L1455 region. This deviation is not confirmed in the IRAM 30 m observation.
[e] The $J = 3-2$ line of $HN^{13}C$ was not observed for this source. The columns are marked with –.

R_D(HNC) is derived from the uncertainties of the column densities of DNC and $HN^{13}C$ for the given H_2 density.

Rosolowsky et al. (2008) reported a typical gas kinetic temperature of 11 K toward the Perseus molecular cloud by observing NH_3 with the 31″ beam, in which they assumed the LTE condition and fitted the hyperfine components of (1,1) and (2,2) lines to derive the gas kinetic temperature. Since our observation beam (10″–20″) is smaller, the kinetic temperature is expected to be higher than 11 K. For safety, we have also evaluated the column densities by assuming the kinetic temperature of 10 and 30 K, and we confirm that the column densities do not significantly vary from those derived by assuming 20 K (the value changes systematically by ∼30%). Hence, the discussion in the following sections should be robust in the condition of the H_2 density of the emitting region for the $J = 1-0$ line between 3×10^4 and 3×10^5 cm^{-3}, that for the $J = 3-2$ line between 1×10^5 and 1×10^7 cm^{-3}, and the gas kinetic temperature between 10 and 30 K. Usually, star-forming cores in molecular clouds would satisfy these conditions (e.g., Hacar et al. 2017).

In the following discussions, we include the variation of the column density and the deuterium ratio due to the assumption of the H_2 density in their uncertainties. Since the fitting and calibration errors of the column density derived for each H_2 density are much smaller than the systematic error due to the assumption of the H_2 density, the uncertainties of N(DNC) and $N(HN^{13}C)$ are estimated from the column densities for the highest and lowest H_2 densities. For the uncertainty of R_D(HNC), we

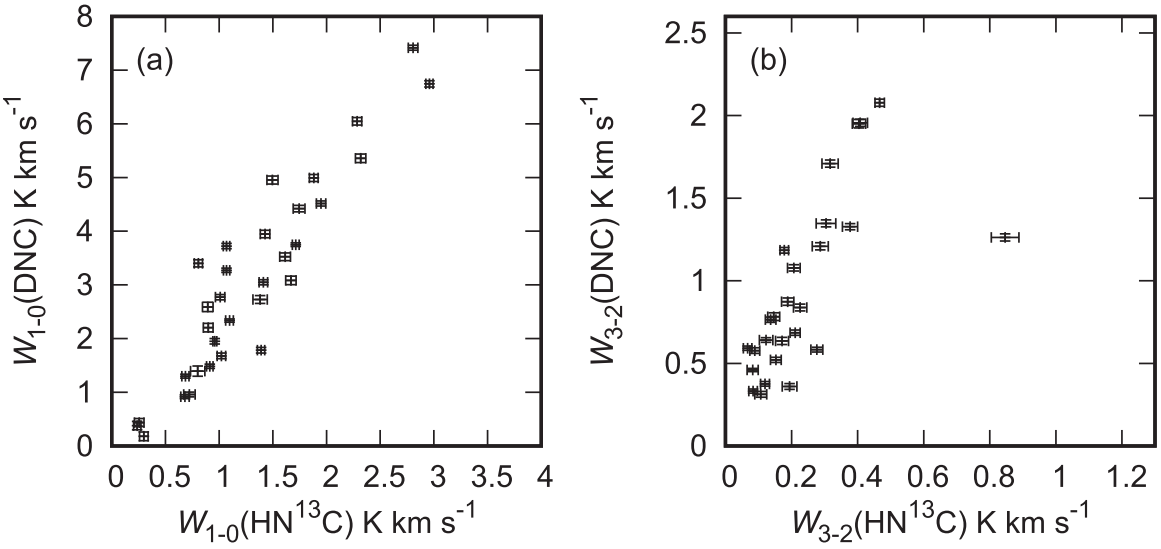

Figure 1. Correlation diagrams of the integrated intensities of DNC and HN^{13}C for the $J = 1-0$ lines (a), and the $J = 3-2$ lines (b).

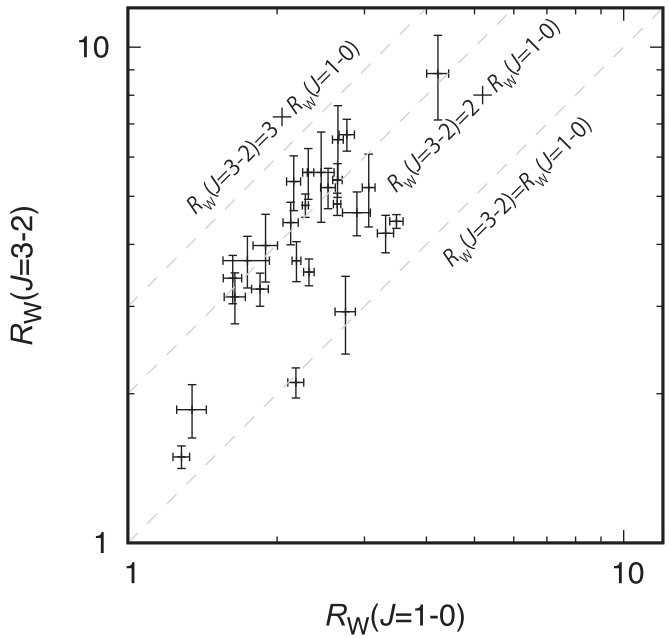

Figure 2. Comparison of the integrated intensity ratio, R_W, between the $J = 1-0$ and $J = 3-2$ lines. The gray dashed lines denote the relations that $R_W(J = 3-2) = R_W(J = 1-0)$, $R_W(J = 3-2) = 2 \times R_W(J = 1-0)$, and $R_W(J = 3-2) = 3 \times R_W(J = 1-0)$.

consider: (1) the uncertainties of the line parameters evaluated by the fitting procedure, (2) the uncertainty of the intensity calibration, and (3) the uncertainty caused by the assumption of the H_2 density. For R_D(HNC) derived from the $J = 3-2$ data, the calibration uncertainty (~20%) is dominant over the other two because the uncertainty caused by the assumption of the H_2 density is almost cancelled out due to the same H_2 density assumed for DNC and HN^{13}C. For R_D(HNC) derived from the $J = 1-0$ data, the assumption of the H_2 density does not significantly contribute to the uncertainty of R_D(HNC) for the same reason. Moreover, the DNC and HN^{13}C lines ($J = 1-0$) are simultaneously observed and, hence, the calibration error should not contribute to the uncertainty of R_D(HNC) either. Nevertheless, we find a daily variation of the intensity calibration between the LSB (for DNC) and USB (for HN^{13}C) data by 11%. Hence, we include the 11% uncertainty for R_D(HNC).

4. Analysis and Discussion

4.1. Deuterium Ratios

The deuterium ratios derived by the LVG analysis in Section 3.3 are listed in Table 5. The mean N(DNC)/N(HN^{13}C) ratio is 2.9 with the standard deviation of 1.2 for the $J = 1-0$ line, while it is 3.4 with a standard deviation of 1.2 for the $J = 3-2$ line. By using the ^{12}C/^{13}C isotopic ratio of 60 (Section 3.3), the mean N(DNC)/N(HNC) ratio (R_D(HNC)) is evaluated to be 0.049 with a standard deviation of 0.020 for the $J = 1-0$ line and 0.056 with a standard deviation of 0.020 for the $J = 3-2$ line. Hirota et al. (2001) reported a similar R_D(HNC) (0.02–0.1) for low-mass protostellar sources in nearby molecular clouds (e.g., Ophiuchus, Taurus, and Perseus molecular clouds). The mean ratios obtained in this study are also comparable to $R_D(N_2H^+)$ of 0.08 with a standard deviation of 0.04 for low-mass star-forming cores in the Perseus molecular cloud complex reported by Friesen et al. (2013). Meanwhile, they are higher than that reported for high-mass star-forming cores; i.e., 0.009 (Fontani et al. 2014). The significant difference between low-mass and high-mass star-forming cores may reflect the environmental differences, such as the gas kinetic temperature and the effects of nearby protostellar sources, in addition to the duration time of the starless-core and protostellar-core phases.

A caveat on the observed deuterium ratio should be noted here: the R_D(HNC) obtained in this study is a beam-averaged value. It is not obvious that the distribution of the deuterated species is the same as that of the normal species. In fact, the line width of DNC ($J = 3-2$) tends to be slightly narrower than that of HN^{13}C ($J = 3-2$) (Figure 3). To discuss such a small scale difference, we need higher-angular resolution observations. In the following sections, we only discuss the beam-averaged value in the following sections.

Table 5
Column Densities of DNC and $HN^{13}C$ and Deuterium Ratios Derived from LVG Modeling

Source	$n(H_2)$ cm^{-3}	N(DNC) $(J=1-0)$ $/10^{12}$ cm^{-2}	$N(HN^{13}C)$ $(J=1-0)$ $/10^{12}$ cm^{-2}	R_D $(J=1-0)$ $/10^2$	$n(H_2)$ cm^{-3}	N(DNC) $(J=3-2)$ $/10^{12}$ cm^{-2}	$N(HN^{13}C)$ $(J=3-2)$ $/10^{12}$ cm^{-2}	R_D $(J=3-2)$ $/10^2$
NGC 1333-1	3×10^4	$14.99^{+0.92}_{-0.86}$	$6.15^{+0.38}_{-0.47}$	$4.06^{+0.40}_{-0.34}$	1×10^5	$38.03^{+3.14}_{-2.90}$	$9.51^{+0.99}_{-0.90}$	$6.67^{+0.84}_{-0.86}$
	1×10^5	$5.80^{+0.36}_{-0.22}$	$2.43^{+0.20}_{-0.14}$	$3.98^{+0.34}_{-0.36}$	3×10^5	$10.92^{+0.90}_{-1.03}$	$2.90^{+0.30}_{-0.32}$	$6.28^{+0.87}_{-0.88}$
	3×10^5	$4.22^{+0.17}_{-0.24}$	$1.63^{+0.10}_{-0.09}$	$4.31^{+0.30}_{-0.36}$	1×10^7	$1.29^{+0.11}_{-0.10}$	$0.24^{+0.02}_{-0.02}$	$9.06^{+1.20}_{-1.17}$
NGC 1333-2	3×10^4	$10.71^{+0.65}_{-0.62}$	$8.96^{+0.36}_{-0.18}$	$1.99^{+0.13}_{-0.14}$	1×10^5	$35.83^{+2.20}_{-1.39}$	$25.59^{+2.11}_{-1.94}$	$2.33^{+0.23}_{-0.21}$
	1×10^5	$4.31^{+0.26}_{-0.17}$	$3.26^{+0.07}_{-0.06}$	$2.20^{+0.14}_{-0.10}$	3×10^5	$10.29^{+0.63}_{-0.40}$	$7.35^{+0.45}_{-0.56}$	$2.33^{+0.23}_{-0.17}$
	3×10^5	$3.14^{+0.13}_{-0.12}$	$2.11^{+0.04}_{-0.08}$	$2.48^{+0.14}_{-0.11}$	1×10^7	$1.19^{+0.05}_{-0.07}$	$0.59^{+0.04}_{-0.05}$	$3.33^{+0.29}_{-0.28}$
NGC 1333-3	3×10^4	$41.16^{+1.67}_{-2.38}$	$6.93^{+0.42}_{-0.53}$	$9.90^{+0.85}_{-0.83}$	1×10^5	$69.42^{+2.83}_{-2.71}$	$18.28^{+1.11}_{-1.05}$	$6.33^{+0.45}_{-0.46}$
	1×10^5	$12.30^{+0.50}_{-0.48}$	$2.47^{+0.15}_{-0.10}$	$8.29^{+0.47}_{-0.60}$	3×10^5	$21.84^{+0.89}_{-1.26}$	$5.15^{+0.32}_{-0.20}$	$7.07^{+0.40}_{-0.60}$
	3×10^5	$7.80^{+0.16}_{-0.30}$	$1.60^{+0.10}_{-0.06}$	$8.13^{+0.36}_{-0.59}$	1×10^7	$2.11^{+0.09}_{-0.08}$	$0.42^{+0.03}_{-0.02}$	$8.45^{+0.47}_{-0.61}$
NGC 1333-4	3×10^4	$20.99^{+2.18}_{-1.97}$	$5.68^{+0.35}_{-0.33}$	$6.16^{+0.73}_{-0.69}$	1×10^5	$25.09^{+1.01}_{-0.97}$	$6.66^{+0.41}_{-0.38}$	$6.28^{+0.44}_{-0.46}$
	1×10^5	$7.21^{+0.59}_{-0.68}$	$2.11^{+0.09}_{-0.12}$	$5.69^{+0.57}_{-0.58}$	3×10^5	$7.21^{+0.29}_{-0.28}$	$1.99^{+0.12}_{-0.11}$	$6.04^{+0.42}_{-0.44}$
	3×10^5	$4.85^{+0.40}_{-0.37}$	$1.37^{+0.06}_{-0.08}$	$5.92^{+0.60}_{-0.51}$	1×10^7	$0.83^{+0.03}_{-0.03}$	$0.16^{+0.01}_{-0.01}$	$8.57^{+0.54}_{-0.63}$
NGC 1333-5	3×10^4	$28.82^{+1.17}_{-1.11}$	$6.93^{+0.42}_{-0.53}$	$6.94^{+0.60}_{-0.50}$	1×10^5	$16.23^{+0.65}_{-0.63}$	$4.57^{+0.68}_{-0.75}$	$5.92^{+1.00}_{-0.91}$
	1×10^5	$9.51^{+0.19}_{-0.37}$	$2.47^{+0.15}_{-0.10}$	$6.41^{+0.28}_{-0.46}$	3×10^5	$4.85^{+0.10}_{-0.19}$	$1.37^{+0.23}_{-0.20}$	$5.92^{+0.87}_{-1.04}$
	3×10^5	$6.27^{+0.25}_{-0.24}$	$1.60^{+0.10}_{-0.06}$	$6.53^{+0.37}_{-0.47}$	1×10^7	$0.61^{+0.02}_{-0.01}$	$0.11^{+0.02}_{-0.02}$	$9.01^{+1.45}_{-1.46}$
NGC 1333-6	3×10^4	$4.66^{+0.28}_{-0.36}$	$3.68^{+0.23}_{-0.21}$	$2.11^{+0.18}_{-0.21}$	1×10^5	$8.78^{+0.72}_{-0.67}$	$7.21^{+1.07}_{-1.06}$	$2.03^{+0.34}_{-0.34}$
	1×10^5	$2.07^{+0.13}_{-0.16}$	$1.48^{+0.06}_{-0.08}$	$2.33^{+0.20}_{-0.20}$	3×10^5	$2.68^{+0.16}_{-0.20}$	$2.15^{+0.32}_{-0.28}$	$2.07^{+0.30}_{-0.35}$
	3×10^5	$1.57^{+0.10}_{-0.12}$	$0.98^{+0.06}_{-0.04}$	$2.68^{+0.20}_{-0.26}$	1×10^7	$0.34^{+0.02}_{-0.02}$	$0.18^{+0.02}_{-0.02}$	$3.19^{+0.46}_{-0.48}$
NGC 1333-7	3×10^4	$34.44^{+2.11}_{-1.98}$	$12.80^{+0.78}_{-0.74}$	$4.48^{+0.38}_{-0.37}$	1×10^5	$22.72^{+1.39}_{-1.73}$	$7.96^{+0.49}_{-0.46}$	$4.76^{+0.40}_{-0.46}$
	1×10^5	$11.14^{+0.45}_{-0.64}$	$4.31^{+0.17}_{-0.25}$	$4.31^{+0.30}_{-0.30}$	3×10^5	$6.40^{+0.53}_{-0.37}$	$2.43^{+0.15}_{-0.18}$	$4.40^{+0.49}_{-0.37}$
	3×10^5	$7.35^{+0.30}_{-0.42}$	$2.68^{+0.11}_{-0.15}$	$4.58^{+0.32}_{-0.32}$	1×10^7	$0.77^{+0.06}_{-0.04}$	$0.20^{+0.01}_{-0.01}$	$6.50^{+0.66}_{-0.55}$
NGC 1333-8	3×10^4	$22.72^{+2.87}_{-2.94}$	$8.61^{+0.71}_{-0.81}$	$4.40^{+0.69}_{-0.67}$	1×10^5	$20.58^{+1.70}_{-1.56}$	$5.46^{+0.57}_{-0.51}$	$6.28^{+0.79}_{-0.81}$
	1×10^5	$7.96^{+0.83}_{-0.75}$	$3.20^{+0.26}_{-0.24}$	$4.15^{+0.53}_{-0.52}$	3×10^5	$5.91^{+0.49}_{-0.45}$	$1.66^{+0.17}_{-0.19}$	$5.92^{+0.82}_{-0.77}$
	3×10^5	$5.57^{+0.46}_{-0.52}$	$2.11^{+0.17}_{-0.16}$	$4.40^{+0.49}_{-0.55}$	1×10^7	$0.71^{+0.06}_{-0.04}$	$0.14^{+0.01}_{-0.01}$	$8.74^{+1.10}_{-1.04}$
NGC 1333-9[a]	3×10^4	*	*	*	1×10^5	*	*	*
	1×10^5	*	*	*	3×10^5	*	*	*
	3×10^5	*	*	*	1×10^7	*	*	*
NGC 1333-10[a]	3×10^4	*	*	*	1×10^5	*	*	*
	1×10^5	*	*	*	3×10^5	*	*	*
	3×10^5	*	*	*	1×10^7	*	*	*
NGC 1333-11	3×10^4	$34.44^{+3.59}_{-2.62}$	$4.85^{+0.50}_{-0.37}$	$11.84^{+1.53}_{-1.53}$	1×10^5	$14.70^{+1.21}_{-1.12}$	$2.33^{+0.57}_{-0.56}$	$10.51^{+2.69}_{-2.68}$
	1×10^5	$10.71^{+0.88}_{-0.82}$	$1.84^{+0.15}_{-0.14}$	$9.71^{+1.09}_{-1.09}$	3×10^5	$4.31^{+0.26}_{-0.33}$	$0.70^{+0.17}_{-0.17}$	$10.31^{+2.57}_{-2.63}$
	3×10^5	$6.93^{+0.42}_{-0.53}$	$1.21^{+0.07}_{-0.09}$	$9.52^{+0.93}_{-0.93}$	1×10^7	$0.53^{+0.03}_{-0.03}$	$0.08^{+0.00}_{+0.00}$	$11.00^{+0.67}_{-0.63}$
NGC 1333-12[a]	3×10^4	$2.96^{+0.58}_{-0.58}$	$1.24^{+0.21}_{-0.22}$	$3.98^{+1.06}_{-1.04}$	1×10^5	$2.29^{+0.34}_{-0.34}$	*	*
	1×10^5	$1.37^{+0.23}_{-0.24}$	$0.53^{+0.09}_{-0.09}$	$4.31^{+1.02}_{-1.07}$	3×10^5	$0.71^{+0.09}_{-0.10}$	*	*
	3×10^5	$1.04^{+0.20}_{-0.19}$	$0.40^{+0.02}_{-0.01}$	$4.31^{+0.84}_{-0.82}$	1×10^7	$0.09^{+0.01}_{-0.01}$	*	*
NGC 1333-13[a]	3×10^4	$0.99^{+0.29}_{-0.26}$	$1.29^{+0.22}_{-0.17}$	$1.29^{+0.41}_{-0.40}$	1×10^5	$0.92^{+0.12}_{-0.12}$	*	*
	1×10^5	$0.49^{+0.13}_{-0.10}$	$0.56^{+0.07}_{-0.08}$	$1.45^{+0.44}_{-0.34}$	3×10^5	$0.28^{+0.04}_{-0.03}$	*	*
	3×10^5	$0.40^{+0.08}_{-0.01}$	$0.40^{+0.03}_{-0.01}$	$1.67^{+0.33}_{-0.14}$	1×10^7	$0.04^{+0.00}_{-0.00}$	*	*
NGC 1333-14	3×10^4	$17.22^{+1.79}_{-1.93}$	$5.46^{+0.45}_{-0.51}$	$5.26^{+0.74}_{-0.73}$	1×10^5	$11.82^{+0.48}_{-0.46}$	$3.14^{+0.40}_{-0.46}$	$6.28^{+0.95}_{-0.83}$
	1×10^5	$5.91^{+0.62}_{-0.56}$	$2.03^{+0.17}_{-0.15}$	$4.86^{+0.63}_{-0.61}$	3×10^5	$3.46^{+0.14}_{-0.20}$	$0.94^{+0.12}_{-0.12}$	$6.16^{+0.83}_{-0.85}$
	3×10^5	$4.06^{+0.33}_{-0.31}$	$1.31^{+0.11}_{-0.08}$	$5.15^{+0.52}_{-0.58}$	1×10^7	$0.42^{+0.02}_{-0.02}$	$0.08^{+0.01}_{-0.00}$	$8.84^{+0.37}_{-0.81}$
NGC 1333-15[a]	3×10^4	$1.24^{+0.24}_{-0.22}$	*	*	1×10^5	$7.96^{+0.49}_{-0.31}$	*	*
	1×10^5	$0.61^{+0.12}_{-0.11}$	*	*	3×10^5	$2.38^{+0.10}_{-0.09}$	*	*
	3×10^5	$0.48^{+0.08}_{-0.09}$	*	*	1×10^7	$0.30^{+0.01}_{-0.01}$	*	*
L1448-1	3×10^4	$141.60^{+7.27}_{-5.46}$	$28.82^{+0.58}_{-1.11}$	$8.19^{+0.53}_{-0.36}$	1×10^5	$58.04^{+2.96}_{-2.82}$	$14.99^{+1.24}_{-1.14}$	$6.45^{+0.59}_{-0.62}$
	1×10^5	$38.03^{+2.32}_{-1.48}$	$8.44^{+0.17}_{-0.17}$	$7.51^{+0.48}_{-0.33}$	3×10^5	$16.88^{+1.04}_{-0.97}$	$4.57^{+0.28}_{-0.43}$	$6.16^{+0.69}_{-0.52}$
	3×10^5	$19.40^{+0.78}_{-0.76}$	$4.85^{+0.10}_{-0.10}$	$6.67^{+0.30}_{-0.29}$	1×10^7	$1.91^{+0.08}_{-0.11}$	$0.37^{+0.03}_{-0.02}$	$8.61^{+0.67}_{-0.87}$
L1448-2	3×10^4	$117.20^{+6.02}_{-6.70}$	$30.58^{+1.24}_{-1.19}$	$6.39^{+0.41}_{-0.45}$	1×10^5	$55.40^{+1.11}_{-1.09}$	$14.99^{+1.24}_{-0.86}$	$6.16^{+0.38}_{-0.52}$

Table 5
(Continued)

Source	$n(H_2)$ cm^{-3}	N(DNC) ($J=1-0$) $/10^{12}$ cm^{-2}	$N(HN^{13}C)$ ($J=1-0$) $/10^{12}$ cm^{-2}	R_D ($J=1-0$) $/10^2$	$n(H_2)$ cm^{-3}	N(DNC) ($J=3-2$) $/10^{12}$ cm^{-2}	$N(HN^{13}C)$ ($J=3-2$) $/10^{12}$ cm^{-2}	R_D ($J=3-2$) $/10^2$
	1×10^5	$31.82^{+1.95}_{-1.84}$	$8.96^{+0.36}_{-0.35}$	$5.92^{+0.43}_{-0.42}$	3×10^5	$16.88^{+1.40}_{-1.28}$	$4.57^{+0.28}_{-0.35}$	$6.16^{+0.69}_{-0.60}$
	3×10^5	$16.88^{+0.68}_{-0.97}$	$5.15^{+0.21}_{-0.20}$	$5.47^{+0.31}_{-0.38}$	1×10^7	$1.91^{+0.12}_{-0.15}$	$0.37^{+0.02}_{-0.03}$	$8.52^{+0.77}_{-0.83}$
L1448-3	3×10^4	$47.28^{+3.90}_{-2.72}$	$14.99^{+0.92}_{-1.14}$	$5.26^{+0.59}_{-0.44}$	1×10^5	$38.79^{+0.78}_{-1.51}$	$14.41^{+1.50}_{-1.36}$	$4.49^{+0.43}_{-0.50}$
	1×10^5	$14.70^{+0.90}_{-0.85}$	$4.95^{+0.30}_{-0.29}$	$4.95^{+0.42}_{-0.42}$	3×10^5	$11.14^{+0.22}_{-0.43}$	$4.22^{+0.44}_{-0.32}$	$4.40^{+0.35}_{-0.49}$
	3×10^5	$9.32^{+0.38}_{-0.54}$	$3.08^{+0.19}_{-0.12}$	$5.05^{+0.28}_{-0.42}$	1×10^7	$1.29^{+0.03}_{-0.05}$	$0.35^{+0.03}_{-0.03}$	$6.15^{+0.54}_{-0.56}$
L1448-4	3×10^4	$41.16^{+3.39}_{-3.88}$	$13.05^{+1.08}_{-0.99}$	$5.26^{+0.59}_{-0.66}$	1×10^5	$15.91^{+0.64}_{-0.62}$	$10.09^{+0.62}_{-0.58}$	$2.63^{+0.19}_{-0.19}$
	1×10^5	$12.30^{+0.76}_{-0.94}$	$4.14^{+0.25}_{-0.24}$	$4.95^{+0.42}_{-0.48}$	3×10^5	$4.57^{+0.18}_{-0.18}$	$2.96^{+0.18}_{-0.17}$	$2.58^{+0.18}_{-0.19}$
	3×10^5	$7.50^{+0.62}_{-0.43}$	$2.52^{+0.15}_{-0.15}$	$4.95^{+0.50}_{-0.42}$	1×10^7	$0.56^{+0.02}_{-0.02}$	$0.24^{+0.01}_{-0.01}$	$3.84^{+0.24}_{-0.25}$
L1448-5	3×10^4	$73.45^{+8.49}_{-7.62}$	$17.57^{+1.82}_{-1.97}$	$6.97^{+1.12}_{-1.02}$	1×10^5	$14.99^{+0.92}_{-0.86}$	$3.68^{+0.72}_{-0.66}$	$6.80^{+1.29}_{-1.38}$
	1×10^5	$20.58^{+2.15}_{-1.94}$	$5.35^{+0.44}_{-0.50}$	$6.41^{+0.90}_{-0.80}$	3×10^5	$4.39^{+0.18}_{-0.25}$	$1.12^{+0.19}_{-0.20}$	$6.54^{+1.20}_{-1.19}$
	3×10^5	$11.59^{+0.96}_{-0.88}$	$3.08^{+0.25}_{-0.23}$	$6.28^{+0.70}_{-0.71}$	1×10^7	$0.54^{+0.03}_{-0.03}$	$0.09^{+0.02}_{-0.01}$	$9.76^{+1.48}_{-1.78}$
IC 348-1	3×10^4	$69.88^{+5.04}_{-5.35}$	$11.59^{+1.21}_{-1.09}$	$10.05^{+1.19}_{-1.30}$	1×10^5	$35.83^{+1.45}_{-0.70}$	$10.50^{+1.09}_{-0.99}$	$5.69^{+0.58}_{-0.60}$
	1×10^5	$19.40^{+1.59}_{-1.13}$	$3.75^{+0.31}_{-0.29}$	$8.62^{+0.97}_{-0.87}$	3×10^5	$10.50^{+0.42}_{-0.41}$	$3.08^{+0.32}_{-0.29}$	$5.69^{+0.58}_{-0.63}$
	3×10^5	$11.14^{+0.68}_{-0.64}$	$2.33^{+0.14}_{-0.18}$	$7.97^{+0.78}_{-0.67}$	1×10^7	$1.19^{+0.02}_{-0.05}$	$0.25^{+0.02}_{-0.02}$	$7.81^{+0.69}_{-0.80}$
IC 348-2	3×10^4	$9.32^{+1.17}_{-1.04}$	$3.53^{+0.45}_{-0.46}$	$4.40^{+0.79}_{-0.74}$	1×10^5	$16.88^{+0.68}_{-0.97}$	$5.46^{+0.69}_{-0.61}$	$5.15^{+0.61}_{-0.71}$
	1×10^5	$3.60^{+0.38}_{-0.34}$	$1.42^{+0.18}_{-0.16}$	$4.23^{+0.65}_{-0.66}$	3×10^5	$4.85^{+0.20}_{-0.28}$	$1.66^{+0.21}_{-0.21}$	$4.86^{+0.66}_{-0.68}$
	3×10^5	$2.63^{+0.22}_{-0.25}$	$0.96^{+0.12}_{-0.11}$	$4.58^{+0.64}_{-0.72}$	1×10^7	$0.58^{+0.02}_{-0.02}$	$0.14^{+0.02}_{-0.02}$	$7.17^{+0.92}_{-0.95}$
IC 348-3[a]	3×10^4	$1.63^{+0.44}_{-0.42}$	$1.14^{+0.22}_{-0.21}$	$2.38^{+0.77}_{-0.77}$	1×10^5	$2.24^{+0.38}_{-0.37}$	*	*
	1×10^5	$0.78^{+0.21}_{-0.19}$	$0.51^{+0.09}_{-0.09}$	$2.58^{+0.83}_{-0.76}$	3×10^5	$0.70^{+0.12}_{-0.11}$	*	*
	3×10^5	$0.62^{+0.15}_{-0.15}$	$0.40^{+0.02}_{-0.01}$	$2.58^{+0.63}_{-0.63}$	1×10^7	$0.09^{+0.02}_{-0.01}$	*	*
IC 348-4	3×10^4	$32.46^{+3.37}_{-2.48}$	$13.58^{+0.83}_{-0.79}$	$3.98^{+0.47}_{-0.39}$	1×10^5	$19.78^{+0.80}_{-0.76}$	$7.07^{+0.58}_{-0.67}$	$4.67^{+0.48}_{-0.42}$
	1×10^5	$9.89^{+0.82}_{-0.75}$	$4.31^{+0.26}_{-0.25}$	$3.83^{+0.39}_{-0.37}$	3×10^5	$5.68^{+0.23}_{-0.22}$	$2.11^{+0.17}_{-0.16}$	$4.49^{+0.39}_{-0.41}$
	3×10^5	$6.27^{+0.52}_{-0.36}$	$2.63^{+0.11}_{-0.15}$	$3.98^{+0.40}_{-0.28}$	1×10^7	$0.66^{+0.03}_{-0.03}$	$0.17^{+0.01}_{-0.01}$	$6.30^{+0.55}_{-0.58}$
B5	3×10^4	$24.12^{+1.98}_{-1.85}$	$6.79^{+0.27}_{-0.13}$	$5.92^{+0.50}_{-0.51}$	1×10^5	$7.65^{+0.96}_{-0.86}$	$4.06^{+0.70}_{-0.73}$	$3.14^{+0.69}_{-0.64}$
	1×10^5	$7.96^{+0.66}_{-0.46}$	$2.43^{+0.05}_{-0.05}$	$5.47^{+0.46}_{-0.33}$	3×10^5	$2.33^{+0.24}_{-0.26}$	$1.21^{+0.24}_{-0.22}$	$3.21^{+0.66}_{-0.72}$
	3×10^5	$5.35^{+0.33}_{-0.21}$	$1.57^{+0.03}_{-0.06}$	$5.69^{+0.41}_{-0.25}$	1×10^7	$0.30^{+0.03}_{-0.03}$	$0.10^{+0.02}_{-0.02}$	$4.95^{+1.03}_{-1.00}$
B1-1	3×10^4	$96.08^{+10.07}_{-9.10}$	$22.72^{+2.37}_{-2.54}$	$7.05^{+1.08}_{-0.99}$	1×10^5	$52.20^{+4.31}_{-4.92}$	$11.14^{+0.92}_{-1.05}$	$7.81^{+0.98}_{-0.98}$
	1×10^5	$26.63^{+2.20}_{-2.51}$	$6.79^{+0.71}_{-0.64}$	$6.54^{+0.82}_{-0.92}$	3×10^5	$15.60^{+1.62}_{-1.75}$	$3.26^{+0.34}_{-0.31}$	$7.97^{+1.12}_{-1.22}$
	3×10^5	$14.41^{+1.19}_{-1.10}$	$3.98^{+0.33}_{-0.38}$	$6.04^{+0.76}_{-0.68}$	1×10^7	$1.70^{+0.14}_{-0.16}$	$0.27^{+0.02}_{-0.02}$	$10.51^{+1.25}_{-1.32}$
B1-2	3×10^4	$76.43^{+8.00}_{-7.24}$	$23.64^{+1.45}_{-1.37}$	$5.39^{+0.64}_{-0.61}$	1×10^5	$21.41^{+2.23}_{-2.02}$	$5.46^{+0.69}_{-0.71}$	$6.53^{+1.09}_{-1.03}$
	1×10^5	$21.41^{+2.23}_{-1.63}$	$7.07^{+0.29}_{-0.41}$	$5.05^{+0.60}_{-0.43}$	3×10^5	$6.15^{+0.64}_{-0.58}$	$1.63^{+0.21}_{-0.21}$	$6.28^{+1.04}_{-0.99}$
	3×10^5	$12.30^{+1.01}_{-0.94}$	$3.98^{+0.24}_{-0.15}$	$5.15^{+0.47}_{-0.50}$	1×10^7	$0.75^{+0.06}_{-0.07}$	$0.13^{+0.02}_{-0.02}$	$9.37^{+1.38}_{-1.48}$
B1-3[a]	3×10^4	$21.41^{+1.76}_{-2.02}$	$9.14^{+0.75}_{-0.70}$	$3.90^{+0.44}_{-0.49}$	1×10^5	$4.75^{+0.60}_{-0.53}$	*	*
	1×10^5	$7.35^{+0.45}_{-0.42}$	$3.20^{+0.26}_{-0.18}$	$3.83^{+0.32}_{-0.39}$	3×10^5	$1.48^{+0.15}_{-0.17}$	*	*
	3×10^5	$5.05^{+0.31}_{-0.29}$	$2.07^{+0.13}_{-0.16}$	$4.06^{+0.40}_{-0.34}$	1×10^7	$0.19^{+0.02}_{-0.02}$	*	*
B1-4	3×10^4	$60.19^{+3.70}_{-3.49}$	$15.29^{+1.26}_{-1.16}$	$6.56^{+0.64}_{-0.66}$	1×10^5	$31.20^{+1.26}_{-1.22}$	$7.80^{+0.98}_{-1.01}$	$6.67^{+0.90}_{-0.88}$
	1×10^5	$17.22^{+0.70}_{-0.99}$	$4.75^{+0.29}_{-0.36}$	$6.04^{+0.52}_{-0.51}$	3×10^5	$8.96^{+0.18}_{-0.35}$	$2.33^{+0.35}_{-0.26}$	$6.41^{+0.73}_{-0.98}$
	3×10^5	$9.89^{+0.60}_{-0.38}$	$2.79^{+0.23}_{-0.16}$	$5.92^{+0.50}_{-0.54}$	1×10^7	$1.04^{+0.04}_{-0.02}$	$0.19^{+0.02}_{-0.03}$	$8.89^{+1.21}_{-1.04}$
B1-5	3×10^4	$48.23^{+3.97}_{-4.54}$	$11.59^{+1.21}_{-1.09}$	$6.94^{+0.87}_{-0.98}$	1×10^5	$35.83^{+2.20}_{-2.72}$	$6.66^{+0.41}_{-0.38}$	$8.97^{+0.75}_{-0.88}$
	1×10^5	$14.13^{+1.16}_{-1.08}$	$3.68^{+0.30}_{-0.28}$	$6.41^{+0.72}_{-0.72}$	3×10^5	$10.50^{+0.86}_{-0.80}$	$1.99^{+0.12}_{-0.11}$	$8.80^{+0.88}_{-0.86}$
	3×10^5	$8.61^{+0.53}_{-0.66}$	$2.24^{+0.18}_{-0.17}$	$6.41^{+0.63}_{-0.72}$	1×10^7	$1.17^{+0.07}_{-0.07}$	$0.16^{+0.01}_{-0.01}$	$11.88^{+1.00}_{-1.00}$
L1455-1	3×10^4	$7.35^{+0.77}_{-0.69}$	$3.90^{+0.24}_{-0.30}$	$3.14^{+0.41}_{-0.35}$	1×10^5	$8.28^{+0.51}_{-0.63}$	$3.14^{+0.47}_{-0.51}$	$4.40^{+0.77}_{-0.73}$
	1×10^5	$3.08^{+0.25}_{-0.29}$	$1.54^{+0.09}_{-0.12}$	$3.33^{+0.37}_{-0.37}$	3×10^5	$2.47^{+0.15}_{-0.14}$	$0.94^{+0.16}_{-0.14}$	$4.40^{+0.70}_{-0.80}$
	3×10^5	$2.24^{+0.18}_{-0.17}$	$1.02^{+0.06}_{-0.06}$	$3.68^{+0.37}_{-0.36}$	1×10^7	$0.31^{+0.02}_{-0.02}$	$0.08^{+0.01}_{-0.00}$	$6.54^{+0.34}_{-0.85}$
L1455-2	3×10^4	$8.78^{+1.11}_{-0.83}$	$5.68^{+0.23}_{-0.33}$	$2.58^{+0.36}_{-0.26}$	1×10^5	$13.58^{+1.12}_{-0.79}$	$5.91^{+0.88}_{-0.87}$	$3.83^{+0.64}_{-0.61}$
	1×10^5	$3.60^{+0.38}_{-0.34}$	$2.11^{+0.09}_{-0.08}$	$2.84^{+0.32}_{-0.29}$	3×10^5	$4.06^{+0.25}_{-0.23}$	$1.77^{+0.26}_{-0.26}$	$3.83^{+0.61}_{-0.61}$
	3×10^5	$2.63^{+0.27}_{-0.20}$	$1.39^{+0.06}_{-0.05}$	$3.14^{+0.35}_{-0.27}$	1×10^7	$0.51^{+0.03}_{-0.03}$	$0.15^{+0.02}_{-0.02}$	$5.83^{+0.88}_{-0.94}$
L1455-3	3×10^4	$10.50^{+1.56}_{-1.18}$	$6.27^{+0.65}_{-0.48}$	$2.79^{+0.46}_{-0.43}$	1×10^5	$9.51^{+0.58}_{-0.55}$	$4.39^{+0.46}_{-0.49}$	$3.61^{+0.46}_{-0.43}$
	1×10^5	$4.14^{+0.43}_{-0.46}$	$2.33^{+0.19}_{-0.18}$	$2.96^{+0.38}_{-0.41}$	3×10^5	$2.84^{+0.17}_{-0.16}$	$1.31^{+0.14}_{-0.12}$	$3.61^{+0.41}_{-0.43}$
	3×10^5	$2.96^{+0.31}_{-0.28}$	$1.51^{+0.12}_{-0.11}$	$3.27^{+0.42}_{-0.41}$	1×10^7	$0.35^{+0.02}_{-0.02}$	$0.11^{+0.01}_{-0.01}$	$5.47^{+0.59}_{-0.58}$
L1455-4[a]	3×10^4	$4.75^{+0.39}_{-0.36}$	$4.14^{+0.34}_{-0.24}$	$1.91^{+0.19}_{-0.21}$	1×10^5	$1.37^{+0.23}_{-0.27}$	*	*
	1×10^5	$2.11^{+0.13}_{-0.16}$	$1.63^{+0.10}_{-0.12}$	$2.16^{+0.21}_{-0.21}$	3×10^5	$0.42^{+0.08}_{-0.02}$	*	*
	3×10^5	$1.57^{+0.13}_{-0.09}$	$1.08^{+0.07}_{-0.06}$	$2.43^{+0.24}_{-0.20}$	1×10^7	$0.05^{+0.01}_{-0.01}$	*	*

Table 5
(Continued)

Source	$n(H_2)$ cm^{-3}	N(DNC) ($J=1-0$) $/10^{12}$ cm^{-2}	$N(HN^{13}C)$ ($J=1-0$) $/10^{12}$ cm^{-2}	R_D ($J=1-0$) $/10^2$	$n(H_2)$ cm^{-3}	N(DNC) ($J=3-2$) $/10^{12}$ cm^{-2}	$N(HN^{13}C)$ ($J=3-2$) $/10^{12}$ cm^{-2}	R_D ($J=3-2$) $/10^2$
				Calibration Source				
L1527[b]	3×10^4	$14.41^{+1.50}_{-1.36}$	$6.53^{+0.26}_{-0.25}$	$3.68^{+0.41}_{-0.38}$	1×10^5	$8.78^{+0.36}_{-0.34}$	–	–
	1×10^5	$5.15^{+0.42}_{-0.39}$	$2.33^{+0.09}_{-0.09}$	$3.68^{+0.34}_{-0.32}$	3×10^5	$2.68^{+0.11}_{-0.15}$	–	–
	3×10^5	$3.60^{+0.22}_{-0.27}$	$1.51^{+0.03}_{-0.06}$	$3.98^{+0.29}_{-0.31}$	1×10^7	$0.34^{+0.01}_{-0.01}$	–	–

Notes.
[a] R_D for the $J=1-0$ line and/or R_D for the $J=3-2$ line are not derived for this source because of non-detection. The corresponding results are marked with $*$.
[b] R_D for the $J=3-2$ line is not derived for this source because the $J=3-2$ line of $HN^{13}C$ was not observed. The corresponding results are marked with –.

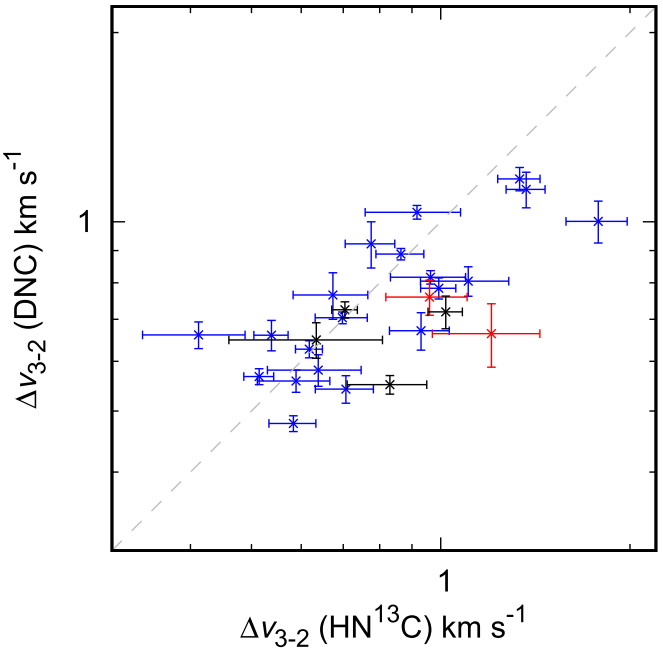

Figure 3. Plots of the line width of the $J=3-2$ lines of DNC and $HN^{13}C$. The gray dotted line indicates the line of $\Delta v_{DNC} = \Delta v_{HN^{13}C}$. The blue and red marks indicate the Class 0 and Class I sources, respectively. The black marks indicate the sources not listed in Tobsin et al. (2016).

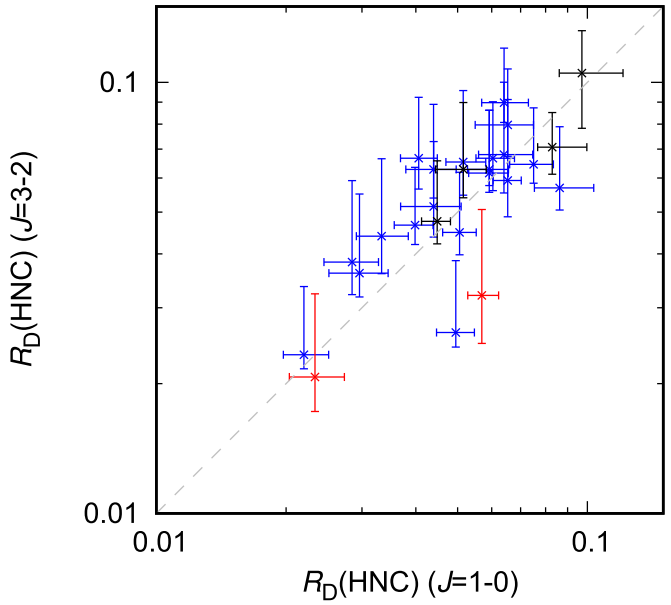

Figure 4. Comparison of the deuterium fractionations derived with $J=1-0$ and $J=3-2$ lines. The gray dashed lines denote the relation that R_D(HNC) is identical for the $J=1-0$ and $J=3-2$ lines. The blue and red marks indicate the Class 0 and Class I sources, respectively. The black marks indicate the sources not listed in Tobin et al. (2016).

4.2. Comparison of Deuterium Ratios Derived from $J=1-0$ and $J=3-2$ Line

Figure 4 shows the comparison between R_D(HNC) derived from the $J=1-0$ and $J=3-2$ lines with the LVG model. Contrary to the comparison in the integrated intensity ratio, R_D(HNC) derived from the $J=3-2$ line is almost comparable to or slightly higher than that from the $J=1-0$ line for most of the sources. Thus, the observed $R_W(3-2)/R_W(1-0)$ ratio of $\sim$2 (Section 3.2) is most likely due to the excitation effect.

In general, the deuterated species would be enhanced in the inner part of the cloud, which is better traced by the $J=3-2$ line. This trend was reported, for instance, by Caselli et al. (2002b) and Crapsi et al. (2005). Caselli et al. (2002b) revealed that the DCO^+/HCO^+ and N_2D^+/N_2H^+ ratios are enhanced around the center of the starless core L1544 due to the heavy depletion of CO onto dust grains. Aikawa et al. (2008) also revealed this trend in their chemical model calculations of dynamically evolving cores. However, this trend is not clearly seen in the comparison of R_D(HNC) for the $J=1-0$ and $J=3-2$ lines, in spite of the differences in their observed beam sizes and critical densities. This may happen because the degree of the deuterium fractionation changes after the onset of star formation, especially in the vicinity of the protostar.

In Figure 4, there are two Class I sources (indicated by red in the figure) in which both the $J=1-0$ lines and $J=3-2$ lines are detected. One of them is approximately on the dashed line, representing that the R_D(HNC) values for the $J=1-0$ and $J=3-2$ lines are identical. The other Class I source appears to lie below the line, i.e., R_D(HNC) for the $J=3-2$ line is lower than that for the $J=1-0$ line. Although most of the Class 0 sources lies on or slightly above the line, a clear trend between the Class 0 and Class I sources cannot be seen because of the large scatters of the plots and a small number of the Class I sources. To assess the dependence of the deuterium ratio on the protosetllar evolution more carefully, we investigate the relation between the deuterium ratio and the bolometric temperature.

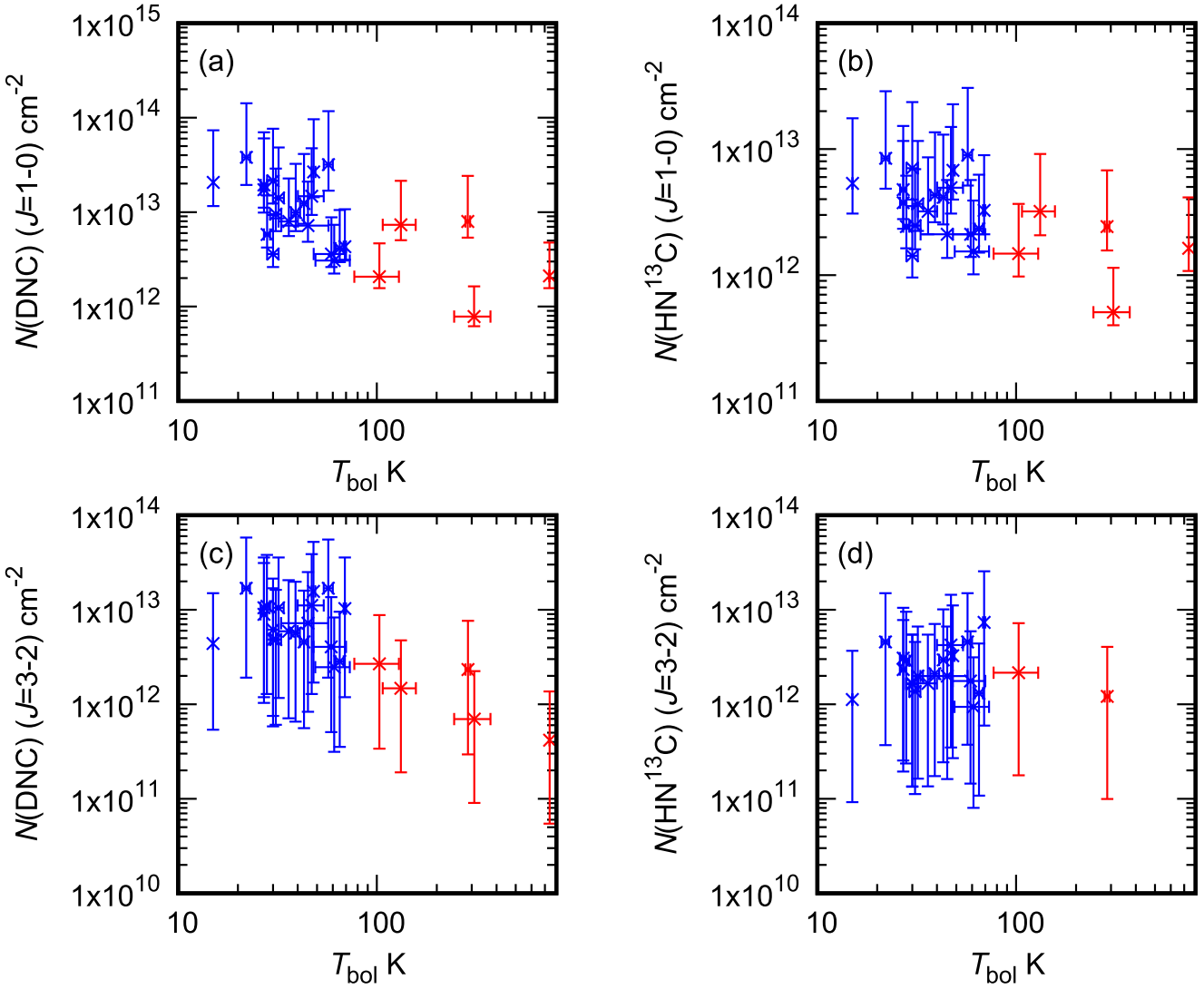

Figure 5. Correlation between bolometric temperature and the column densities of DNC and $HN^{13}C$. The blue and red marks indicate the Class 0 and Class I sources, respectively.

4.3. Deuterium Ratio of HNC versus Bolometric Temperature

It is known that the bolometric temperature (T_{bol}) is an evolutionary indicator of protostars (e.g., Evans et al. 2009). First, we investigated a relation between the column densities of DNC and $HN^{13}C$ and the bolometric temperature (Figure 5). The bolometric temperature is taken from Tobin et al. (2016). In Figure 5, the sources not listed in Tobin et al. (2016) are excluded for a fair comparison, where the excluded sources are shown in Table 1. A clear trend cannot be seen in this plot due to the large uncertainty. Nevertheless, the difference of the mean column densities between the Class 0 and Class I sources is marginally recognized, except for $N(HN^{13}C)$ obtained from the $J = 3-2$ line; as shown in Table 6. Thus, the column densities of DNC (and $HN^{13}C$) could be lower for the Class I sources than that for the Class 0 sources.

The deuterium ratio, R_D(HNC), is also plotted against the bolometric temperature in Figure 6. A negative correlation between the bolometric temperature and the deuterium ratio can be seen both for the $J = 1-0$ and $J = 3-2$ lines, although there is an apparent exception, B5 (Barnard 5 IRS 1). This source is characterized by the distinct outflow emission (Zapata et al. 2014) and, hence, it might be heavily influenced by outflow activities even at a large scale (∼a few 1000 au). In addition, Pineda et al. (2011) reported that this source is embedded in large filaments. The high R_D(HNC) ratio may be attributed to the contribution of a cloud surrounding B5. Without this source, the correlation coefficient is −0.73 for the $J = 1-0$ line and −0.69 for the $J = 3-2$ line. Even with this source, the correlation coefficient is −0.62 for the $J = 1-0$ line and −0.66 for the $J = 3-2$ line. This result means that

Table 6
Mean Column Densities for Class 0 and Class I Sources Derived for the $J = 1-0$ and $J = 3-2$ Lines

	N(DNC)[a] /10^{12} cm^{-2}		$N(HN^{13}C)$[a] /10^{12} cm^{-2}	
	Class 0	Class I	Class 0	Class I
$J = 1-0$	$13.77^{+9.70}_{-1.68}$	$4.05^{+4.35}_{-0.71}$	$4.15^{+2.38}_{-0.43}$	$1.85^{+2.54}_{-0.32}$
$J = 3-2$	$8.23^{+5.02}_{-1.85}$	$1.52^{+1.78}_{-0.69}$	$2.64^{+1.62}_{-0.63}$	$1.68^{+2.90}_{-1.13}$

Note.
[a] Mean values are derived for the Class 0 and Class I sources.

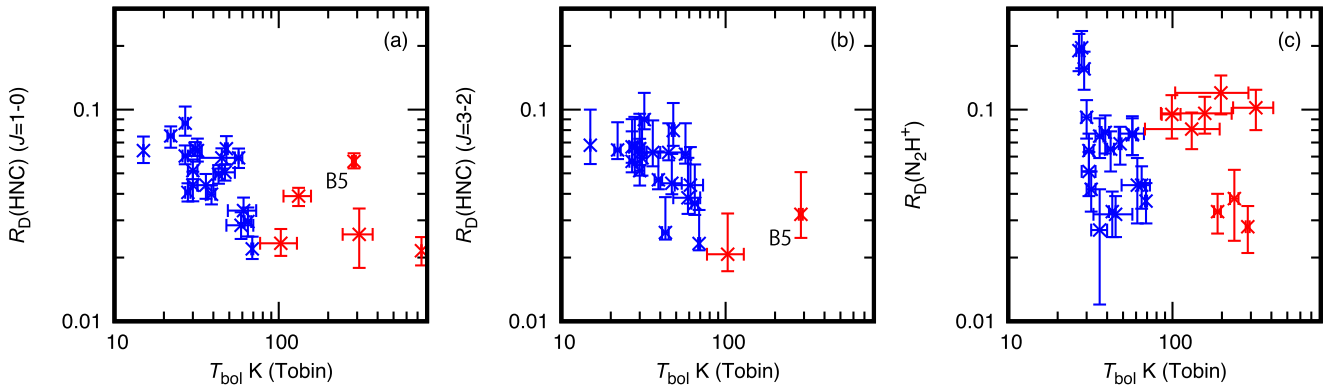

Figure 6. The correlation between bolometric temperature and the deuterium ratio of HNC derived with the $J = 1-0$ lines (a) and the $J = 3-2$ lines (b). The correlation between the bolometric temperature and the deuterium ratio of N_2H^+ is also shown in (c) (Friesen et al. 2013). Note that the bolometric temperature is also taken from Tobin et al. (2016) and the sources not listed in it are excluded for (c), although Friesen et al. (2013) employ the bolometric temperature reported by Enoch et al. (2009). The blue and red marks indicate the Class 0 and Class I sources, respectively.

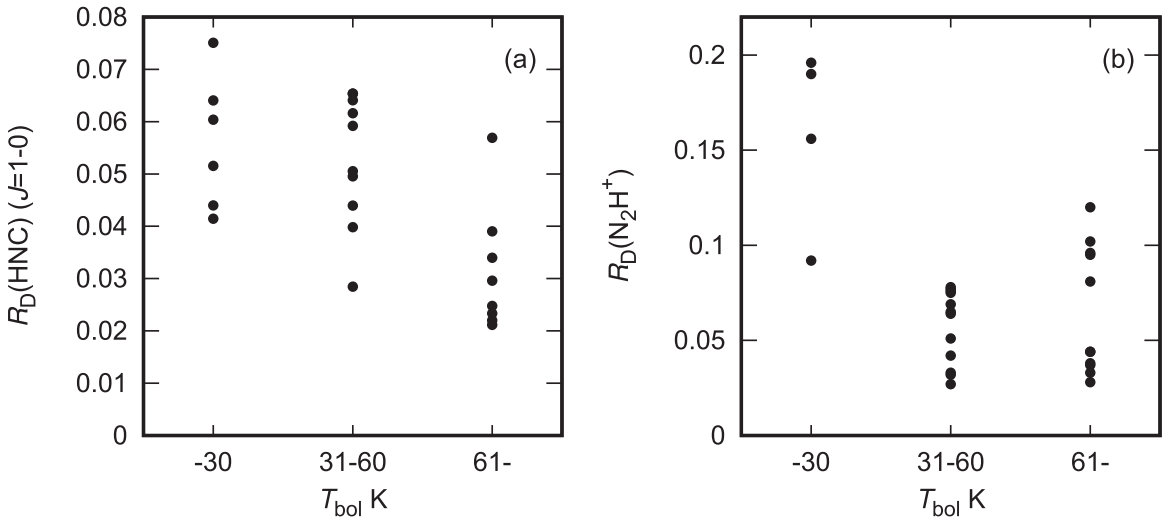

Figure 7. The change in R_D(HNC) (a) and $R_D(N_2H^+)$ (b) against T_{bol}, where we bind T_{bol} into three bins to show different trends of the decrease of the deuterium ratio between the neutral and ionic species. Note that the bolometric temperature is also taken from Tobin et al. (2016) for N_2H^+ in (b). The deuterium ratio of the molecular ion N_2H^+ seems to decrease faster than that of the neutral molecule HNC.

R_D(HNC) is lower for the higher bolometric temperature. Since the bolometric temperature can be regarded as an evolutionary indicator of protostars especially for the Class 0 and I phase (Evans et al. 2009), the negative correlation suggests that R_D(HNC) decreases as the protostar evolves.

4.4. Interpretation of the DNC/HNC Ratio

As noted in Section 4.3, R_D(HNC) seems to decrease along with protostellar evolution. Since the deuterium ratio gradually increases with the chemical evolution in the starless-core phase (Hirota et al. 2011b), the deuterium fractionation is highest just at the onset of star formation.

Friesen et al. (2013) also claimed the negative correlation between $R_D(N_2H^+)$ and the bolometric temperature. We compare the plot between T_{bol} and R_D(HNC) with that between T_{bol} and $R_D(N_2H^+)$ in Figure 6. The negative correlation between $R_D(N_2H^+)$ and T_{bol} (Figure 6(c)) is not as clear as that between R_D(HNC) and T_{bol}. The sources with T_{bol} lower than 60 K show a large span of $R_D(N_2H^+)$ (0.02–0.2). In contrast, R_D(HNC) remains moderate for most of these young sources. This implies that $R_D(N_2H^+)$ decreases faster than R_D(HNC). It should be noted that there are 5 Class I sources with high $R_D(N_2H^+)$ (>0.07). These sources may be affected by the contribution of the cold outer envelope still remaining around the protostars, as was the case of B5 (which was mentioned previously). To see this marginal trend more clearly, we show R_D(HNC) and $R_D(N_2H^+)$ for the three ranges of T_{bol}: $T_{bol} \leqslant 30$ K, 31 K $\leqslant T_{bol} \leqslant 60$ K, and $T_{bol} \geqslant 61$ K (Figure 7). We can confirm the trend that $R_D(N_2H^+)$ decreases faster than R_D(HNC) along with protostellar evolution.

This result is consistent with the expectation that $R_D(N_2H^+)$ approaches the low equilibrium ratio at the elevated temperature in earlier stages than R_D(HNC). This trend reflects the difference of reactivity between the ionic and neutral species. In general, the destruction rate of ionic species is higher than that of neutral species, as mentioned in Section 1. At the elevated temperature after the onset of star formation, N_2H^+ and N_2D^+, formed in the cold phase, are broken up by CO evaporated from dust grains within a shorter period ($\sim 10^{1-2}$ yr) than the duration time of the Class 0 phase (Sakai et al. 2012). Therefore, $R_D(N_2H^+)$ rapidly decreases to the equilibrium value at high temperature. Meanwhile, the destruction of HNC and DNC, formed in the cold phase, slowly proceeds in a timescale of $\sim 10^{4-5}$ yr, which is almost comparable to the duration time

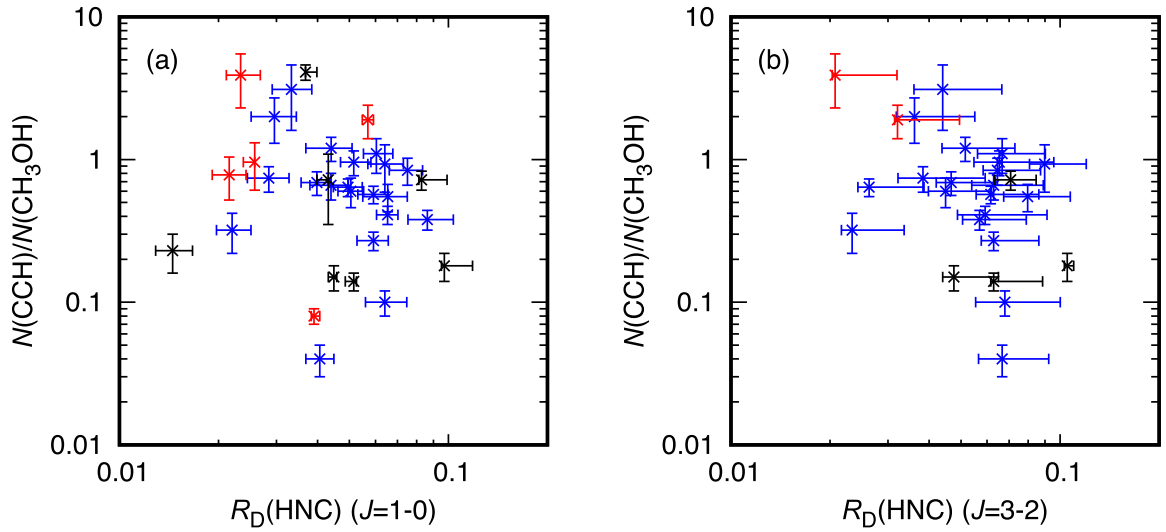

Figure 8. Comparison between the CCH/CH_3OH ratio and R_D(HNC) derived from the $J = 1-0$ line (a) and R_D(HNC) derived from the $J = 3-2$ line (b). The data of the CCH/CH_3OH ratio are taken from Higuchi et al. (2018). The blue and red marks indicate the Class 0 and Class I sources, respectively. The black marks indicate the sources not listed in Tobin et al. (2016).

of the Class 0 phase (Sakai et al. 2012). Hence, R_D(HNC) will gradually decrease along with the protostellar evolution. Furthermore, as noted in Section 4.2, deuterated species tends to be concentrated around the core center compared with normal species before the onset of star formation. Hence, the destruction of DNC and $HN^{13}C$ near the protostar would also contribute to low R_D(HNC) in evolved stages.

The main destruction pathway of HNC and DNC is a reaction with a protonated molecule, HX^+ (X = H_2, CO, N_2, etc.) and a subsequent electron recombination reaction:

$$HNC + HX^+ \rightarrow HNCH^+ + X \quad (10)$$

$$HNCH^+ + e^- \rightarrow HCN + H. \quad (11)$$

A similar scheme is held for DNC. Reaction (10) proceeds if the proton affinity of X is lower than that of HNC (or DNC) (8.00 eV). Another is the neutral-neutral reaction with H (e.g., Graninger et al. 2014):

$$HNC + H \rightarrow HCN + H, \quad (12)$$

$$DNC + H \rightarrow HCN + D. \quad (13)$$

It is reported that these reactions have an activation barrier of 2000 K (Talbi et al. 1996), hence they are unlikely to proceed in the protostellar sources at the temperature of a few 10 K. However, Hirota et al. (1998) suggested that the HNC to HCN conversion occurs at the temperature higher than 24 K on the basis of the observations of $HN^{13}C$ and $H^{13}CN$ in molecular clouds. Therefore, some mechanisms could be responsible for the break up of HNC and DNC in the vicinity of the protostar, although an understanding of these processes is left for future studies.

In our result, a marginal difference of the DNC (and $HN^{13}C$) column densities between the Class 0 and Class I sources is seen. However, large uncertainties in the assumption of the H_2 density make it difficult to test whether DNC and $HN^{13}C$ are really destroyed. Moreover, different sources have different sizes and different amount of gas. Hence, we cannot simply compare the column densities among sources. To figure out the mechanism for the decrease of the deuterium fractionation after the onset of star formation, we need to resolve the distributions of DNC and $HN^{13}C$ in the vicinity of the protostar.

4.5. Deuterium Ratio versus Chemical Composition

So far, this analysis has focused on the relation with T_{bol} which shows that the observed variation of R_D(HNC) would mainly originate from its decrease along with protostellar evolution. However, we cannot rule out the possibility that the initial R_D(HNC) just at the onset of star formation would have already been different from source to source due to the different evolutionary histories of the sources. As one of the tests for this possibility, we compare R_D(HNC) with the CCH/CH_3OH ratio in Figure 8, where the CCH/CH_3OH ratio is taken from Higuchi et al. (2018). The CCH/CH_3OH ratio can be regarded as a good tracer of the chemical characteristics; i.e., the warm carbon-chain chemistry (WCCC)/hot corino chemistry (Sakai & Yamamoto 2013). Hot corino sources tend to show the CH_3OH rich property, while WCCC sources tend to show the CCH rich property. As the origin of the hot corino chemistry and WCCC, the duration time of the starless-core phase is proposed by Sakai et al. (2009). In particular, these authors proposed that the amount of the C atom and the CO molecule depleted onto dust grains would depend on the duration time of the starless-core phase. Since the C atom is gradually converted to CO through gas-phase reactions, CO tends to be depleted onto dust grains for the longer duration time case. This leads to hot corino chemistry via hydrogenation of CO into CH_3OH. Meanwhile, the C atoms will be directly depleted onto dust grains for the shorter duration time case, and they are hydrogenated to form rich CH_4. Evaporation of CH_4 after the onset of star formation leads to WCCC through gas-phase reactions. Since the deuterium fractionation also proceeds in the starless-core phase, its degree could also depend on the duration time of the starless-core phase (Sakai et al. 2009; Hirota et al. 2011b). This mechanism would cause the variation of the deuterium ratio at the onset of star formation among sources. If the variation in starless-core phase is to some extent preserved after the onset of star formation, then it is expected that CH_3OH rich sources show high deuterium ratio. However,

no apparent relation can be seen between the CCH/CH_3OH ratio and R_D(HNC) (Figure 8). This result seems to indicate that the decrease of the deuterium ratio in the protostellar-core phase overwhelms the variation of the deuterium ratio in the starless-core phase.

5. Summary

We observed the $J = 1-0$ and $J = 3-2$ lines of DNC and $HN^{13}C$, and we evaluated the deuterium ratios of HNC with LVG model for 34 Class 0 and Class I protostellar sources in the Perseus molecular cloud complex. The main results are summarized below.

1. Both the $J = 1-0$ and $J = 3-2$ lines of DNC are detected toward 32 protostellar sources out of 34 observed sources, while the $J = 1-0$ and $J = 3-2$ lines of $HN^{13}C$ are detected toward 31 and 26 protostellar sources, respectively.
2. The LVG analysis is applied separately for the $J = 1-0$ lines and $J = 3-2$ lines due to the different beam sizes. The deuterium ratio derived with the $J = 3-2$ lines is almost comparable to that derived with the $J = 1-0$ lines for most of the sources.
3. The column densities of DNC (and $HN^{13}C$) could be lower for the Class I sources than that for the Class 0 sources, although the trend is marginal.
4. Both R_D(HNC) values derived from the $J = 1-0$ lines and $J = 3-2$ lines have negative correlation with the bolometric temperature of the protostar. This indicates that the deuterium ratio decreases after the onset of star formation.
5. We compared the relationship of the deuterium ratio of HNC and N_2H^+ with T_{bol}. Both of the deuterium ratios tend to decrease with the protostellar evolution. However, the decrease of the deuterium ratio of the neutral species, HNC, is slower than that of the ionic species, N_2H^+. This is consistent with the result of the chemical model calculation reported in Sakai et al. (2012).
6. There is no apparent correlation between R_D(HNC) and the CCH/CH_3OH ratio in this survey. This result suggests that the deuterium ratio mostly reflects the process after the onset of the star formation, regardless of the chemical characteristics of the protostellar cores.

The authors are grateful to the anonymous reviewer of this paper for their invaluable comments. The authors are grateful to the IRAM staff for successfully carrying out the IRAM 30 m observations and to the NRO staff for excellent support. The authors thank Yuri Aikawa for precious comments. This study is supported by KAKENHI (25108005, 15J01610, 16H03964, JP18J11010, and 18H05222). The authors acknowledge the financial support by JSPS and MAEE under the Japan–France integrated action programme. This work is supported by JSPS KAKENHI grant No. JP18J11010.

Appendix A
Observed Spectrum

The observed spectra of the $J = 1-0$ and $J = 3-2$ lines of DNC and $HN^{13}C$ are shown in Figures 9–10.

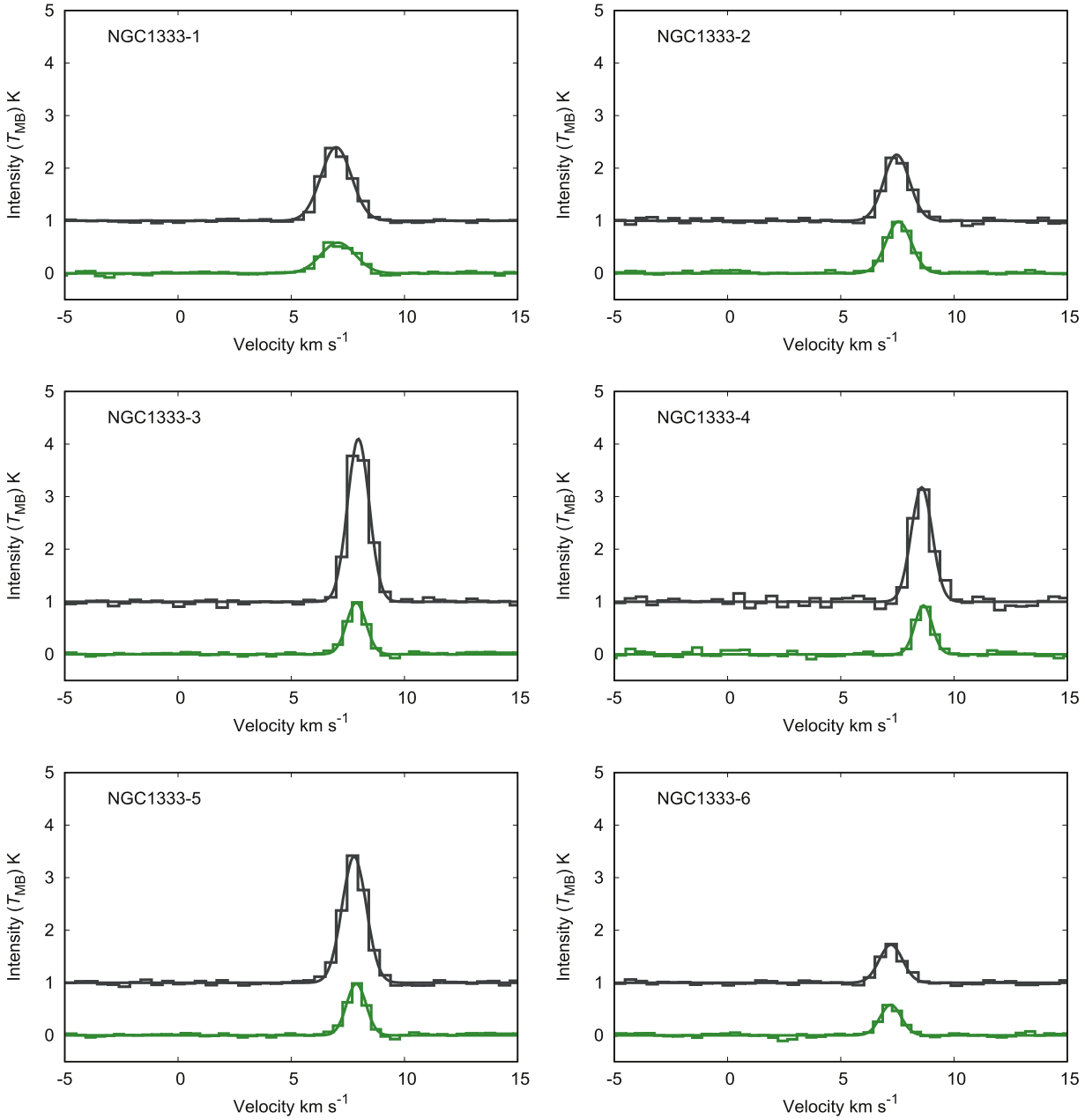

Figure 9. The spectra of the $J = 1-0$ lines of DNC (black) and HN^{13}C (green) overlaid with fitted Gaussian function. The spectra of DNC is offset by 1 K. The velocity for the sources in L1455 is corrected by 10 km s^{-1} (see the footnotes for Tables 3 and 4).

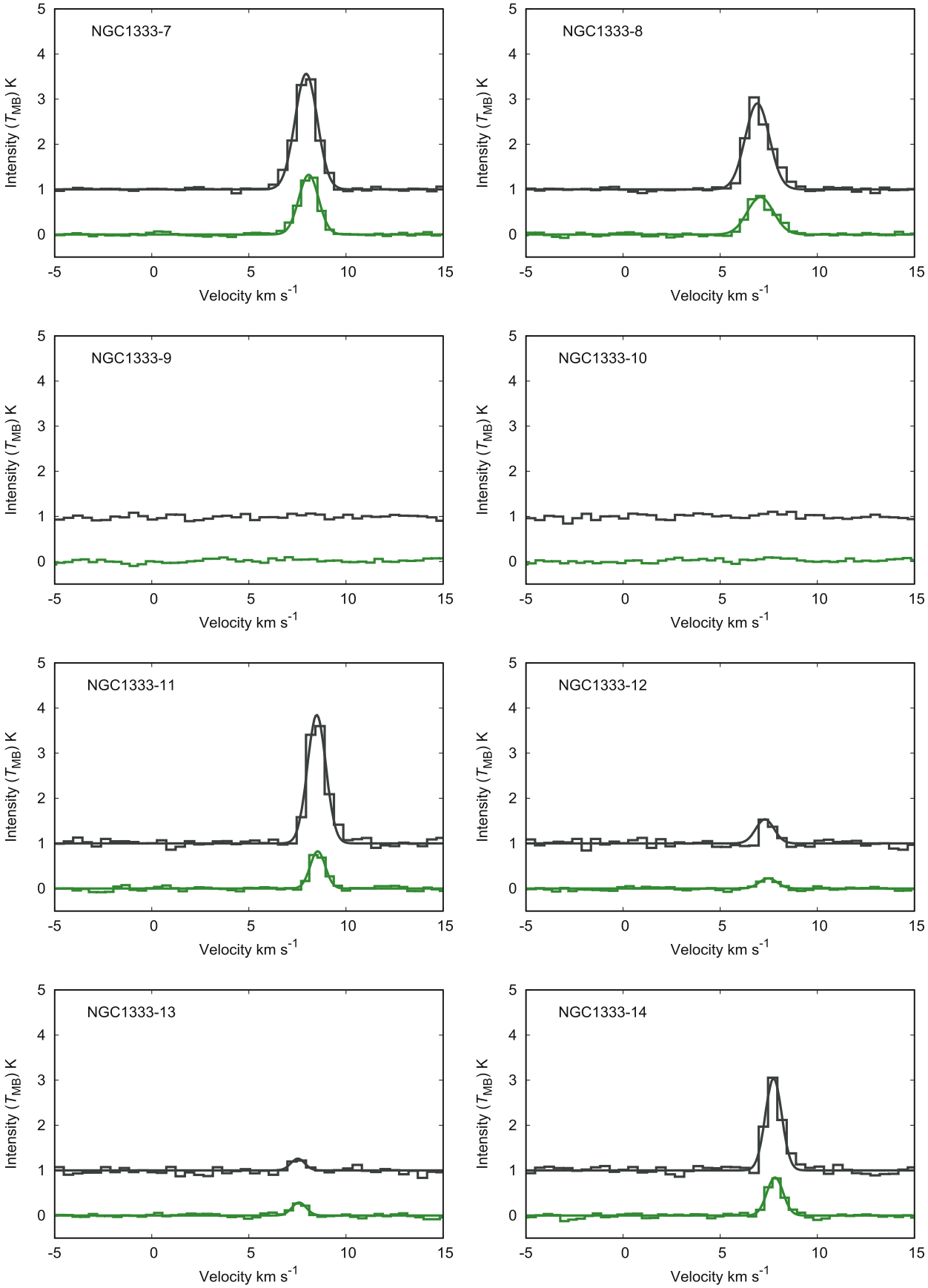

Figure 9. (Continued.)

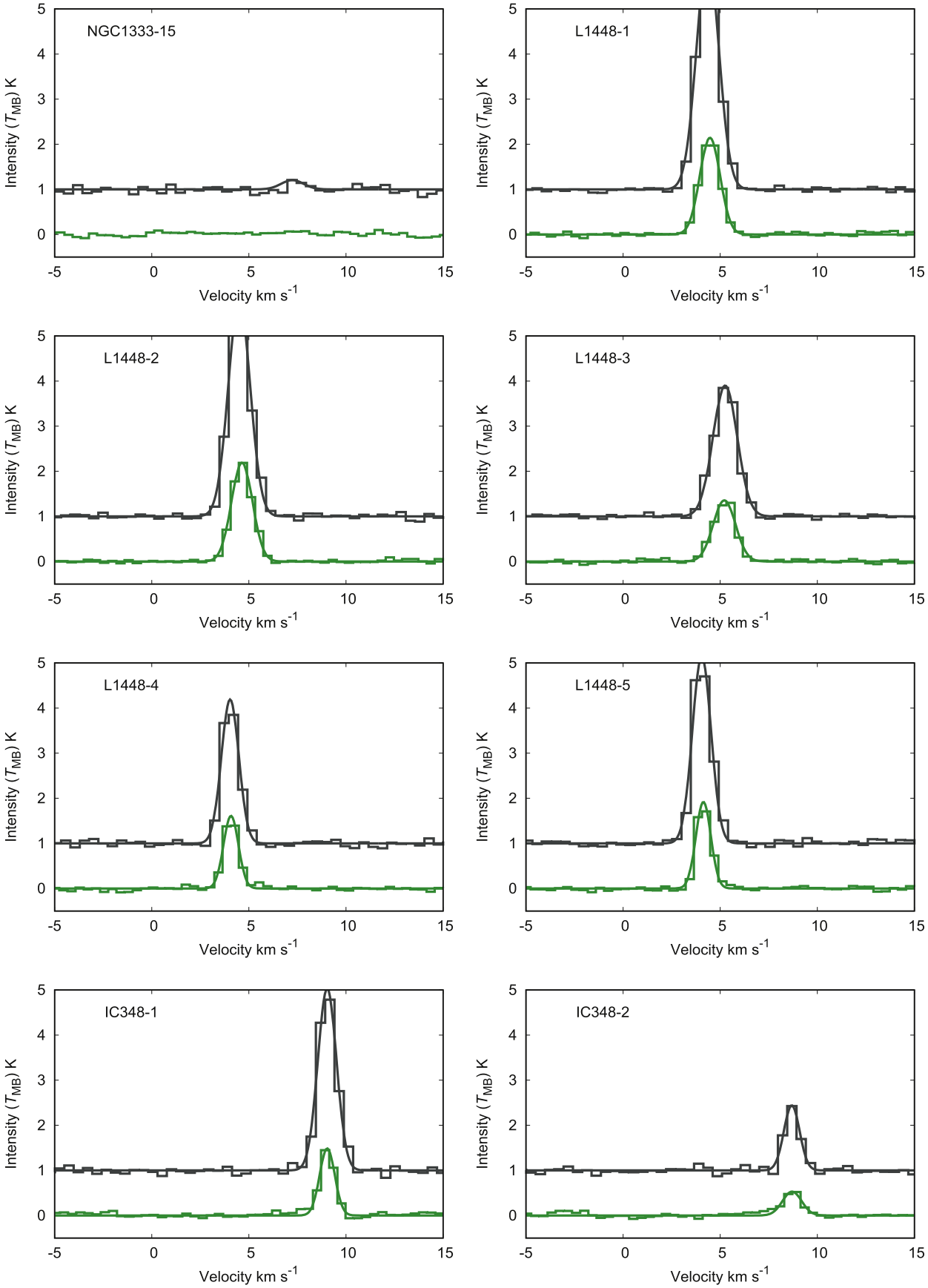

Figure 9. (Continued.)

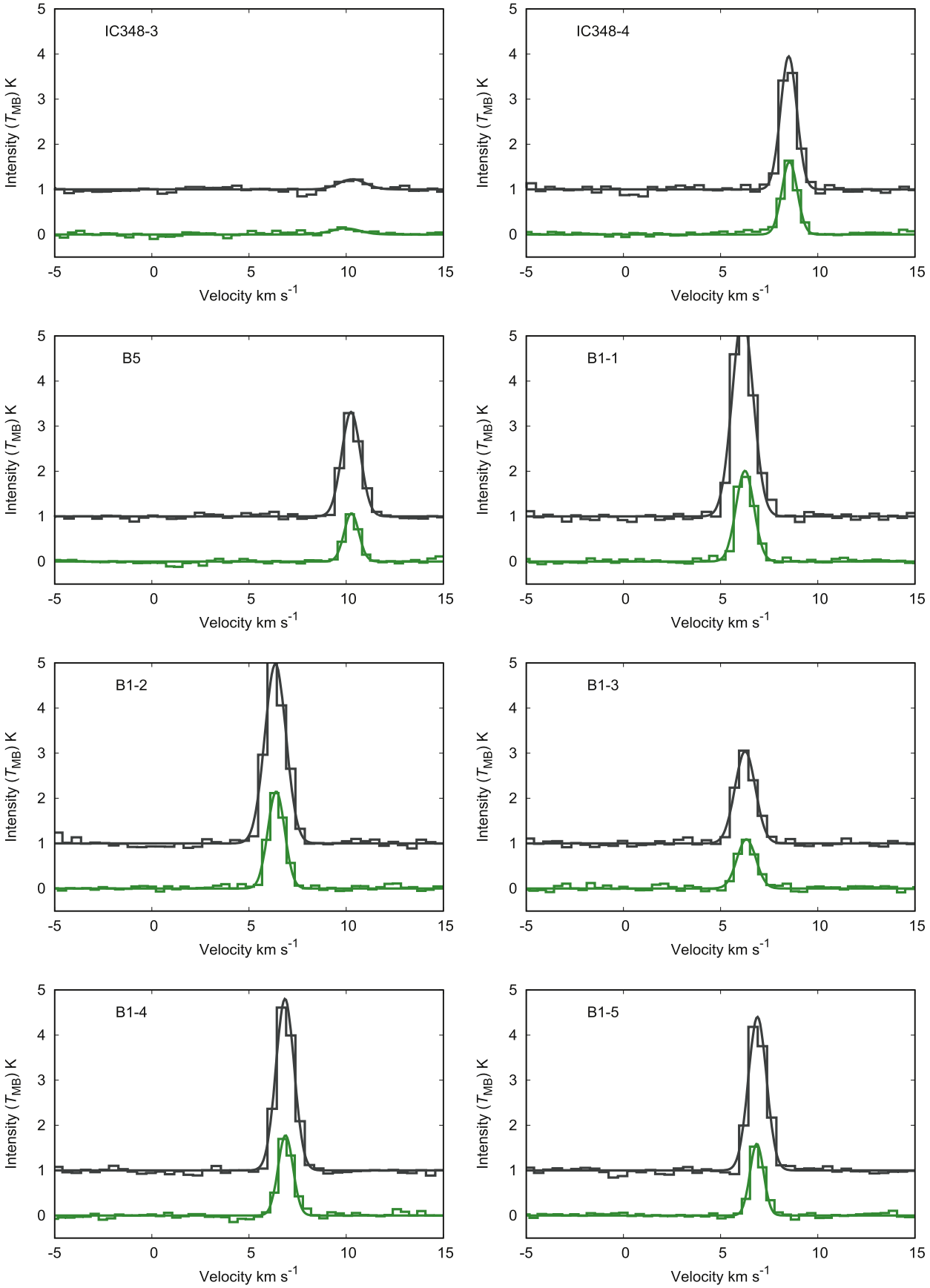

Figure 9. (Continued.)

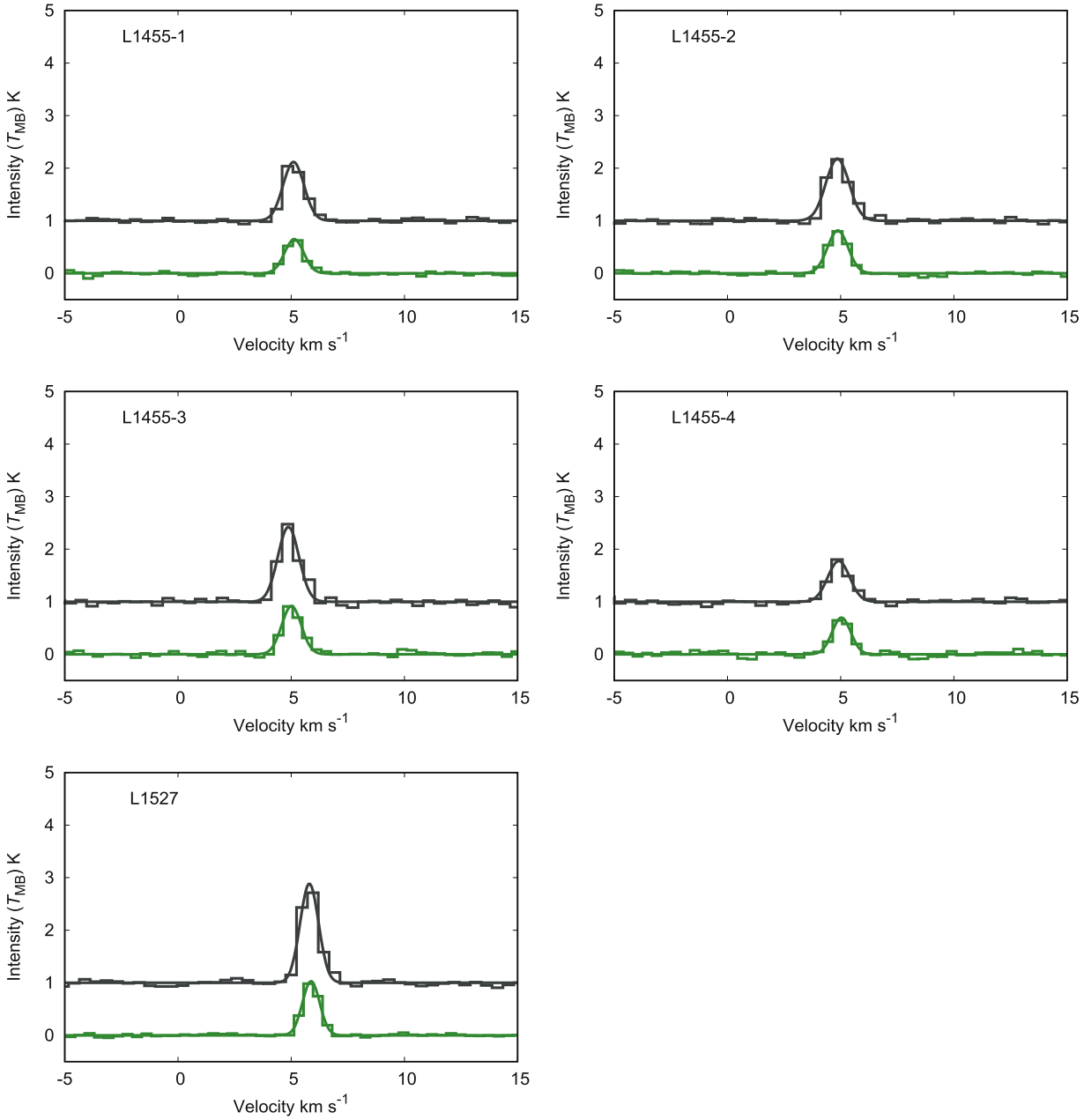

Figure 9. (Continued.)

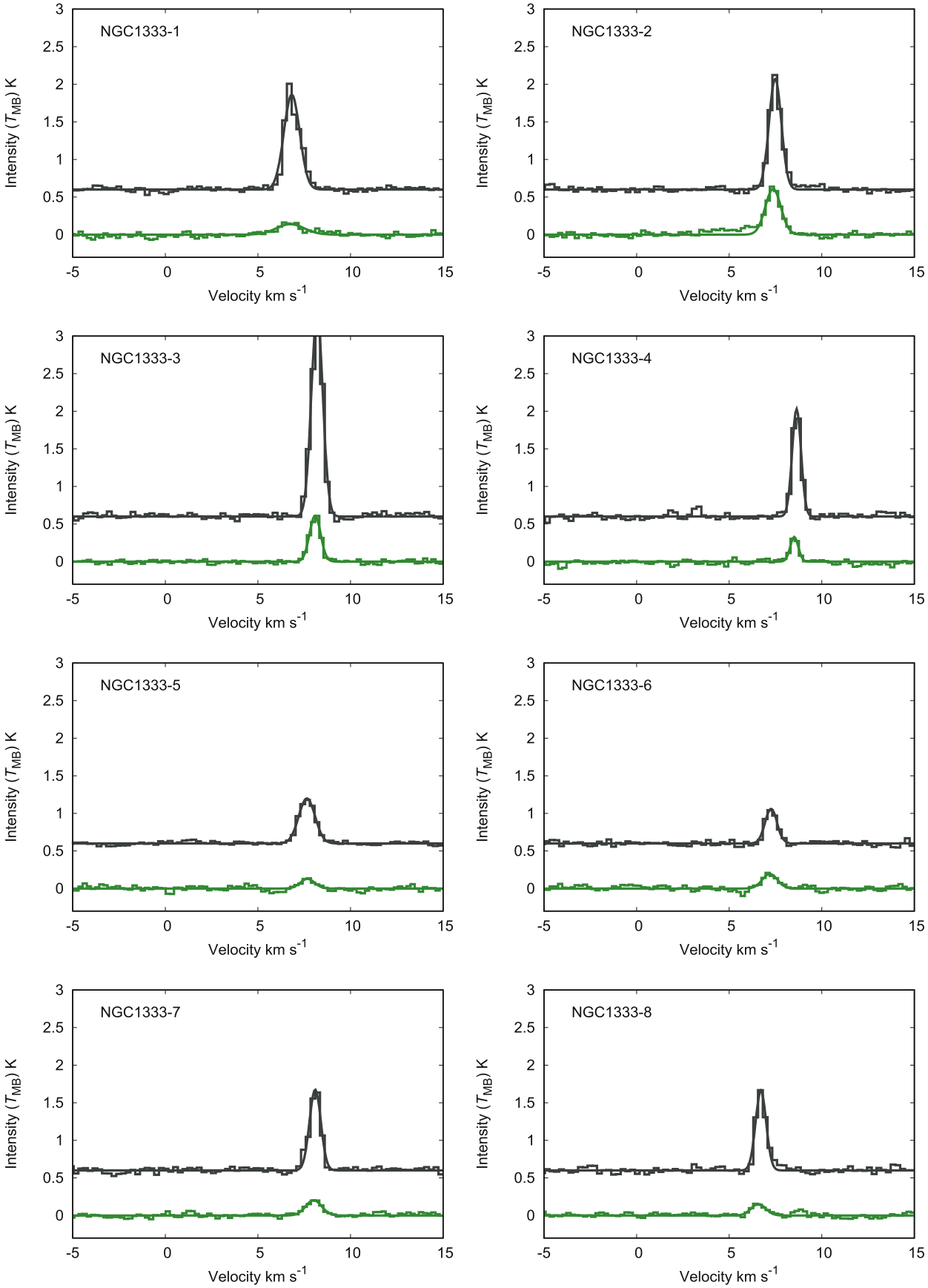

Figure 10. The spectra of the $J = 3-2$ lines of DNC (black) and $HN^{13}C$ (green) overlaid with fitted Gaussian function. The spectra of DNC is offset by 0.6 K.

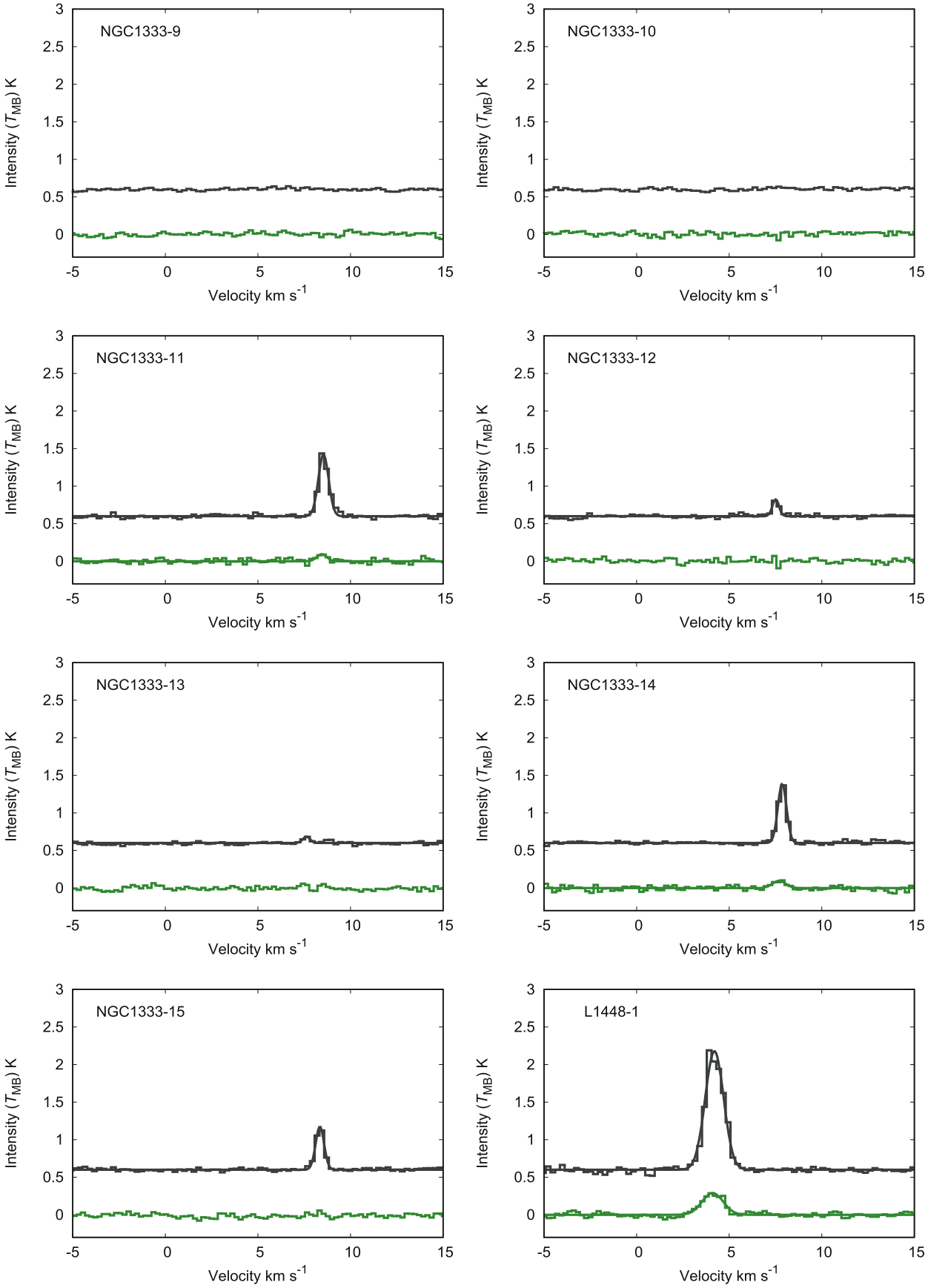

Figure 10. (Continued.)

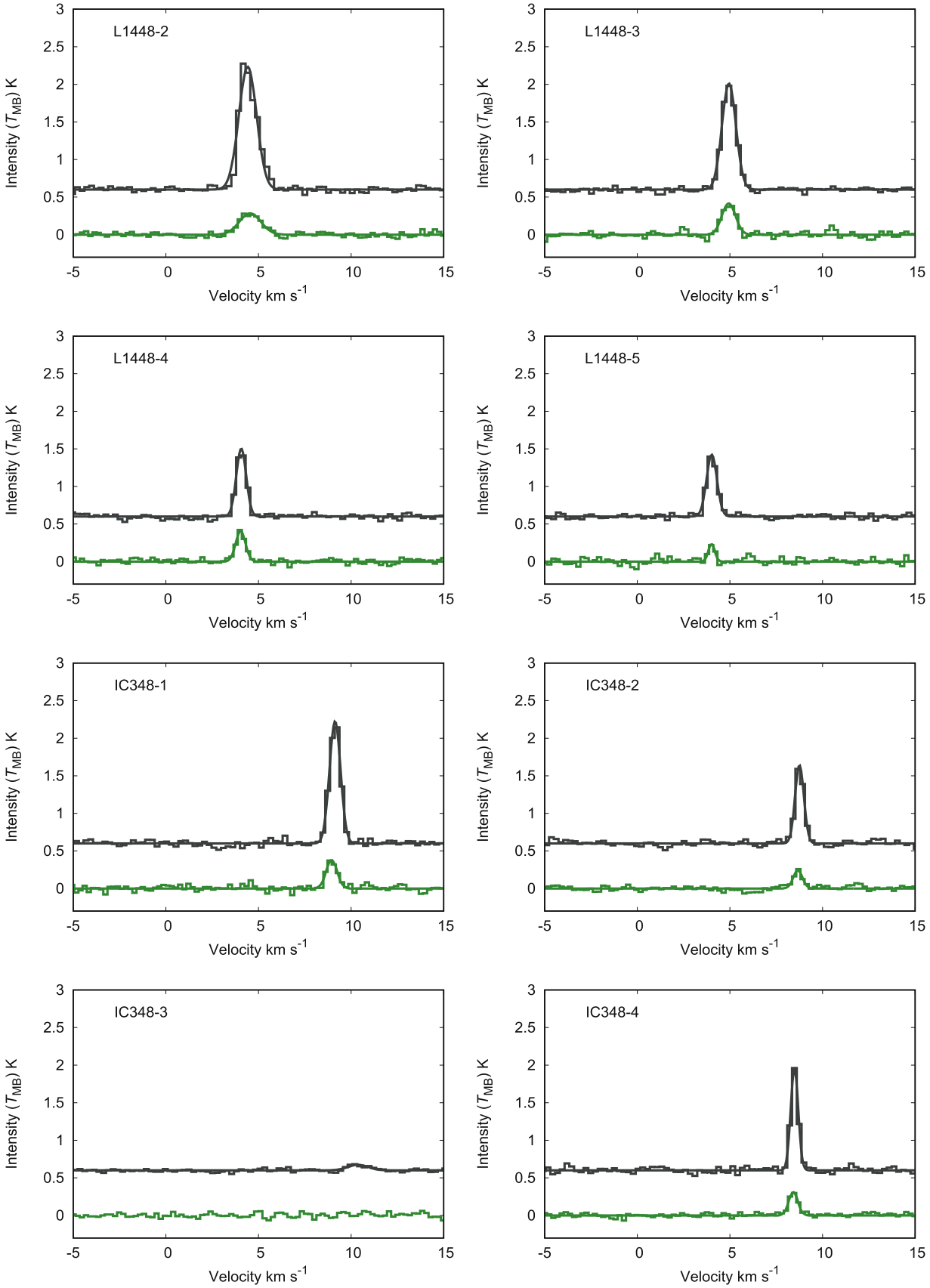

Figure 10. (Continued.)

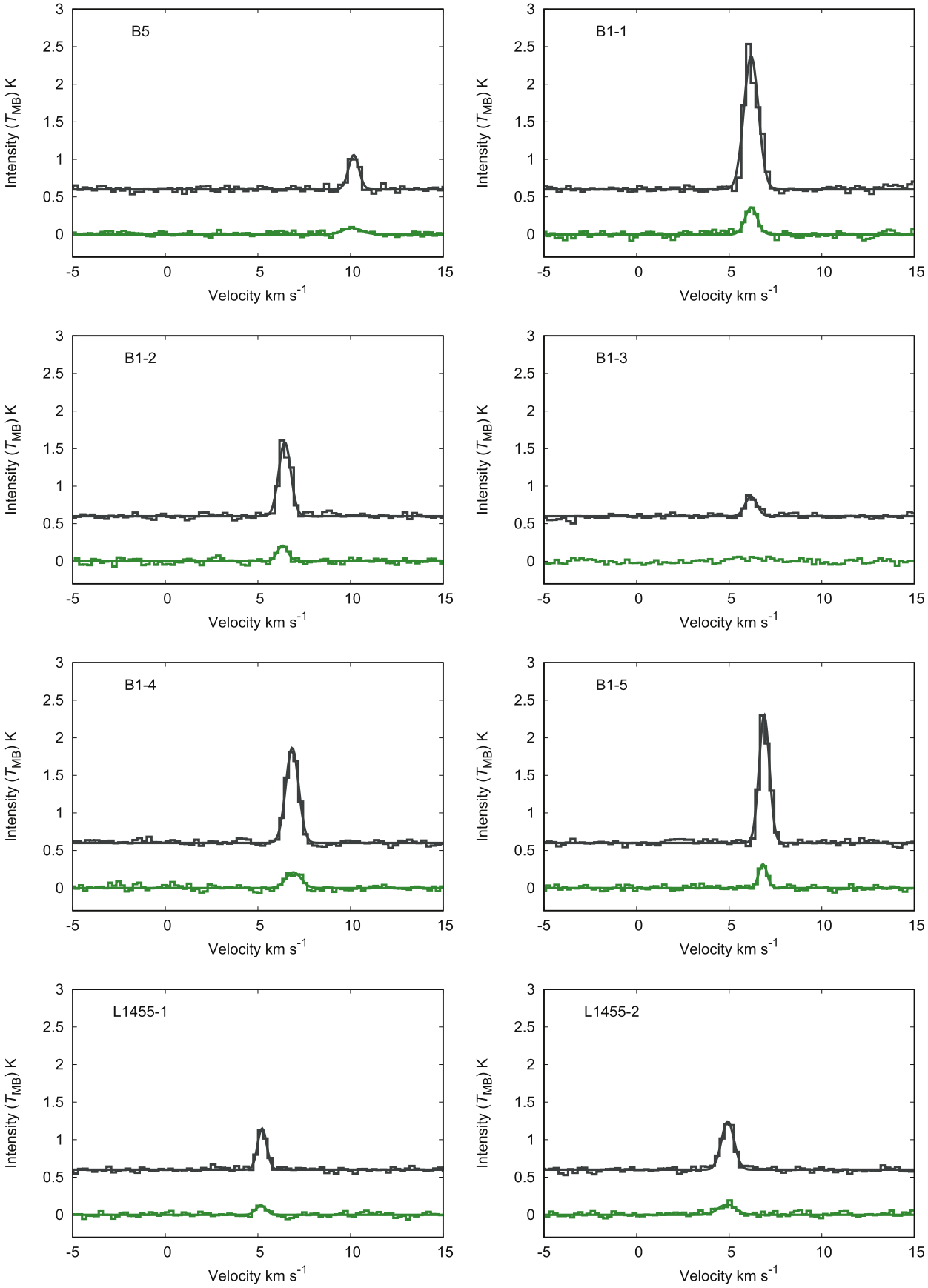

Figure 10. (Continued.)

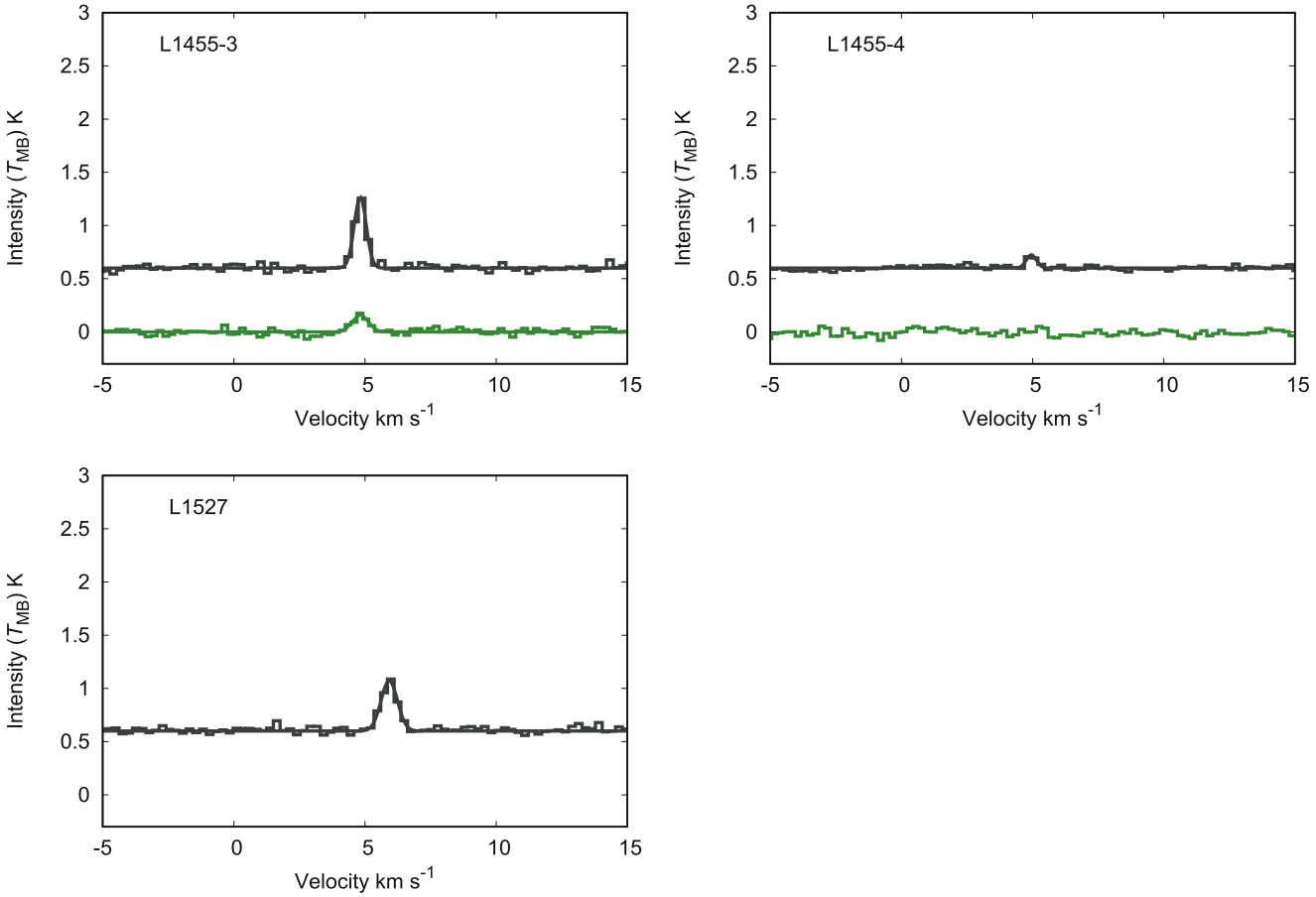

Figure 10. (Continued.)

Appendix B
Hyperfine Splitting

The DNC and HN^{13}C lines are split by the nuclear quadrupole interaction of the ^{14}N and D nuclei, as well as the magnetic hyperfine interaction of the ^{13}C nucleus. The hyperfine structures of the $J = 1-0$ lines of DNC and HN^{13}C are summarized in Table 7.

Table 7
Hyperfine Structures of the $J = 1-0$ Lines of DNC and HN^{13}C[a]

Transition	Quantum Numbers[b] I, F for DNC or F_1, F_2, F for HN^{13}C	Offset km s^{-1}	Relative Intensity
DNC $J = 1-0$	2,1−2,2/2,1−0,0	±0.000	1.00
	1,1−1,1	−0.453	0.99
	2,3−2,2	−0.689	2.33
	1,2−1,1	−0.804	1.67
	2,2−2,2/0,1−0,0/0,1−2,2	−1.091	2.67
	1,0−1,1	−1.279	0.33
HN^{13}C $J = 1-0$	0,1,1−1,2,2	±0.000	1.00
	2,2,2−1,1,1/2,2,2−1,2,2/ 2,2,1−1,1,0/2,2,1−1,2,1	−0.398	4.04
	2,3,3−1,2,2/2,3,2−1,1,1/ 2,3,2−1,2,1	−0.546	6.63
	1,1,1−1,1,1/1,2,2−1,2,1/ 1,2,2−1,2,2	−0.725	3.66

Notes.
[a] Taken from van der Tak et al. (2009).
[b] A coupling scheme of the angular momenta is $I = I(^{14}\mathrm{N})+I(\mathrm{D})$ and $F = J+I$ for DNC, while it is $F_1 = J+I(^{14}\mathrm{N})$, $F_2 = F_1+I(^{13}\mathrm{C})$, and $F = F_2+I(\mathrm{H})$ for HN^{13}C. The quantum number F_2 is a half integer but is rounded up.

Appendix C
LTE Analysis

The integrated intensity ratio of DNC and $HN^{13}C$ (R_W) for the $J = 1-0$ and $J = 3-2$ lines can be calculated under the

Table 8
Excitation Temperature (T_{ex}[a]) and Optical Depth (τ[b]) of DNC and $HN^{13}C$ for the $J = 1-0$ and $J = 3-2$ Lines

	$J = 1-0$				$J = 3-2$			
	DNC		$HN^{13}C$		DNC		$HN^{13}C$	
Source	T_{ex}[a] (K)	τ[a]	T_{ex}[a] (K)	τ[a]	T_{ex}[a] (K)	τ[a]	T_{ex}[a] (K)	τ[a]
NGC 1333-1	6.22	0.55	5.06	0.32	5.53	1.72	4.85	0.17
NGC 1333-2	6.16	0.50	5.25	0.57	5.70	2.10	5.02	0.96
NGC 1333-3	7.15	1.34	5.25	0.56	7.03	4.89	5.01	0.95
NGC 1333-4	6.63	0.91	5.23	0.54	5.67	2.02	4.88	0.45
NGC 1333-5	6.76	1.01	5.25	0.56	5.08	0.68	4.85	0.15
NGC 1333-6	5.91	0.28	5.06	0.33	5.01	0.50	4.86	0.24
NGC 1333-7	6.84	1.09	5.43	0.78	5.37	1.37	4.86	0.26
NGC 1333-8	6.48	0.78	5.17	0.47	5.36	1.36	4.85	0.19
NGC 1333-9[b]	*	*	*	*	*	*	*	*
NGC 1333-10[b]	*	*	*	*	*	*	*	*
NGC 1333-11	7.00	1.22	5.17	0.47	5.21	0.99	4.85	0.11
NGC 1333-12	5.83	0.21	4.90	0.12	4.93	0.22	*	*
NGC 1333-13[b]	5.72	0.10	4.93	0.16	*	*	*	*
NGC 1333-14	6.55	0.84	5.18	0.48	5.18	0.94	4.85	0.11
NGC 1333-15[b]	5.69	0.08	*	*	5.06	0.63	*	*
L1448-1	8.59	2.56	5.91	1.33	5.81	2.32	4.87	0.39
L1448-2	8.31	2.32	5.94	1.35	5.86	2.42	4.87	0.38
L1448-3	7.05	1.25	5.44	0.79	5.66	2.00	4.91	0.59
L1448-4	7.23	1.41	5.59	0.96	5.25	1.10	4.91	0.57
L1448-5	7.85	1.93	5.78	1.18	5.21	1.00	4.86	0.30
IC 348-1	7.76	1.85	5.51	0.87	5.85	2.40	4.90	0.52
IC 348-2	6.24	0.57	5.03	0.29	5.35	1.34	4.86	0.31
IC 348-3[b]	5.70	0.08	4.86	0.07	4.89	0.07	*	*
IC 348-4	7.06	1.26	5.59	0.96	5.60	1.89	4.88	0.42
B5	6.69	0.96	5.29	0.61	5.01	0.49	4.85	0.10
B1-1	8.07	2.11	5.83	1.23	6.01	2.74	4.89	0.49
B1-2	7.72	1.82	5.93	1.34	5.31	1.23	4.86	0.26
B1-3[b]	6.55	0.84	5.30	0.63	4.94	0.27	*	*
B1-4	7.62	1.74	5.69	1.08	5.53	1.73	4.86	0.26
B1-5	7.35	1.51	5.57	0.94	5.93	2.57	4.88	0.43
L1455-1	6.10	0.44	5.09	0.37	5.05	0.61	4.85	0.15
L1455-2	6.12	0.47	5.16	0.46	5.10	0.73	4.85	0.17
L1455-3	6.24	0.57	5.22	0.53	5.11	0.77	4.85	0.20
L1455-4[b]	5.94	0.30	5.11	0.40	4.90	0.12	*	*
				Calibration Source				
L1527[c]	6.47	0.77	5.27	0.59	5.02	0.51	...	...

Notes.
[a] The excitation temperature and the optical depth derived in the LVG analysis to reproduce observed data. The H_2 density is assumed to be $n(H_2) = 1 \times 10^5$ cm^{-3} for the $J = 1-0$ line and $n(H_2) = 3 \times 10^5$ cm^{-3} for the $J = 3-2$ line, while the kinetic temperature is assumed to be 20 K.
[b] T_{ex} and τ for the non-detection line are marked with $*$.
[c] T_{ex} and τ for the non-observed line are marked with –.

LTE condition, as follows. By assuming an optically thin line, $R_{\rm W}$ is represented as:

$$R_{\rm W} = \frac{\exp\left(\frac{h\nu({\rm DNC})}{k_{\rm b}T_{\rm ex}}\right)-1}{\exp\left(\frac{h\nu({\rm HN^{13}C})}{k_{\rm b}T_{\rm ex}}\right)-1}\frac{U({\rm HN^{13}C})}{U({\rm DNC})} \times \frac{\exp\left(-\frac{E_{{\rm u}J}({\rm DNC})}{k_{\rm b}T_{\rm ex}}\right)}{\exp\left(-\frac{E_{{\rm u}J}({\rm HN^{13}C})}{k_{\rm b}T_{\rm ex}}\right)}\frac{N({\rm DNC})}{N({\rm HN^{13}C})}, \quad (14)$$

where ν, U, and $E_{{\rm u},J}$ denote the frequency of the line, the partition function, and the upper state energy of the $J-(J-1)$ transition, respectively, for DNC and $HN^{13}C$, as indicated in parentheses. Here, $S\mu^2$ of DNC and $HN^{13}C$ is assumed to be the same for the same transition. $T_{\rm ex}$ stands for the excitation temperature, $k_{\rm b}$ for the Boltzmann constant, and N for the column density of DNC and $HN^{13}C$. By use of this equation, $R_{\rm W}(3-2)/R_{\rm W}(1-0)$ is represented as:

$$\begin{aligned} &R_{\rm W}(3-2)/R_{\rm W}(1-0) \\ &= \frac{\left(\exp\left(\frac{h\nu_{3-2}({\rm DNC})}{k_{\rm b}T_{\rm ex}}\right)-1\right)\left(\exp\left(\frac{h\nu_{1-0}({\rm HN^{13}C})}{k_{\rm b}T_{\rm ex}}\right)-1\right)}{\left(\exp\left(\frac{h\nu_{3-2}({\rm HN^{13}C})}{k_{\rm b}T_{\rm ex}}\right)-1\right)\left(\exp\left(\frac{h\nu_{1-0}({\rm DNC})}{k_{\rm b}T_{\rm ex}}\right)-1\right)} \\ &\times \exp\left(\frac{(E_{\rm u3}({\rm HN^{13}C})-E_{\rm u3}({\rm DNC}))-(E_{\rm u1}({\rm HN^{13}C})-E_{\rm u1}({\rm DNC}))}{k_{\rm b}T_{\rm ex}}\right) \\ &\simeq \frac{\left(\exp\left(\frac{11.0}{T_{\rm ex}\ {\rm K}}\right)-1\right)\left(\exp\left(\frac{4.18}{T_{\rm ex}\ {\rm K}}\right)-1\right)}{\left(\exp\left(\frac{12.5}{T_{\rm ex}\ {\rm K}}\right)-1\right)\left(\exp\left(\frac{3.66}{T_{\rm ex}\ {\rm K}}\right)-1\right)}\exp\left(\frac{2.59}{T_{\rm ex}\ {\rm K}}\right), \end{aligned} \quad (16)$$

where we employ the classical expression of the partition function for a linear molecule. Here, we assume that the $N({\rm DNC})/N({\rm HN^{13}C})$ ratios traced by the $J=1-0$ and $J=3-2$ lines are identical. Since the difference of the upper state energies between DNC and $HN^{13}C$ is larger for the $J=3-2$ line than for the $J=1-0$ line, the $R_{\rm W}(3-2)/R_{\rm W}(1-0)$ ratio tends to be larger than 1. Indeed, the ratio is 1.5 for $T_{\rm ex}$ of 4.5 K, while it is 1.2 for $T_{\rm ex}$ of 10 K. The excitation temperature derived from LVG analysis is between these values (Table 8). Hence, the observed $R_{\rm W}(3-2)/R_{\rm W}(1-0)$ ratio of 2 that is shown in Figure 2 cannot be reproduced with this effect.

We also note the effect of optical depth. The optical depth of each line derived from LVG analysis is also shown in Table 8. Overall, the $J=3-2$ line satisfies the optically thin ($\tau<1$) condition in all of the sources. For the $J=1-0$ line, the optical depth of DNC tends to be higher than that of $HN^{13}C$, and the DNC line is optically thick ($\tau>1$) in 14 sources. This might contribute the high $R_{\rm W}(3-2)/R_{\rm W}(1-0)$ ratio, to some extent. However, a number of sources show that the high ratio is significantly larger than 14. Hence, the optical depth effect cannot entirely account for the $R_{\rm W}(3-2)/R_{\rm W}(1-0)$ ratio of 2 that is shown in Figure 2.

ORCID iDs

Muneaki Imai https://orcid.org/0000-0002-5342-6262
Nami Sakai https://orcid.org/0000-0002-3297-4497
Aya E. Higuchi https://orcid.org/0000-0002-9221-2910
Yoko Oya https://orcid.org/0000-0002-0197-8751
Yoshimasa Watanabe https://orcid.org/0000-0002-9668-3592
Takeshi Sakai https://orcid.org/0000-0003-4521-7492
Cecilia Ceccarelli https://orcid.org/0000-0001-9664-6292

References

Aikawa, Y., Ohashi, N., Inutsuka, S.-i., Herbst, E., & Takakuwa, S. 2001, ApJ, 552, 639
Aikawa, Y., Wakelam, V., Garrod, R. T., & Herbst, E. 2008, ApJ, 674, 993
Albertsson, T., Semenov, D. A., Vasyunin, A. I., Henning, T., & Herbst, E. 2013, ApJS, 207, 27
Bacmann, A., Lefloch, B., Ceccarelli, C., et al. 2003, ApJL, 585, L55
Caselli, P., & Ceccarelli, C. 2012, A&ARv, 20, 56
Caselli, P., Stantcheva, T., Shalabiea, O., Shematovich, V. I., & Herbst, E. 2002a, P&SS, 50, 1257
Caselli, P., Vastel, C., Ceccarelli, C., et al. 2008, A&A, 492, 703
Caselli, P., Walmsley, C. M., Zucconi, A., et al. 2002b, ApJ, 565, 344
Chen, H.-R., Liu, S.-Y., Su, Y.-N., & Wang, M.-Y. 2011, ApJ, 743, 196
Crapsi, A., Caselli, P., Walmsley, C. M., et al. 2004, A&A, 420, 957
Crapsi, A., Caselli, P., Walmsley, C. M., et al. 2005, ApJ, 619, 379
Dislaire, V., Hily-Blant, P., Faure, A., et al. 2012, A&A, 537, A20
Emprechtinger, M., Caselli, P., Volgenau, N. H., Stutzki, J., & Wiedner, M. C. 2009, A&A, 493, 89
Enoch, M. L., Evans, N. J., II, Sargent, A. I., & Glenn, J. 2009, ApJ, 692, 973
Evans, N. J., II, Dunham, M. M., Jørgensen, J. K., et al. 2009, ApJS, 181, 321
Fontani, F., Palau, A., Caselli, P., et al. 2011, A&A, 529, L7
Fontani, F., Sakai, T., Furuya, K., et al. 2014, MNRAS, 440, 448
Friesen, R. K., Kirk, H. M., & Shirley, Y. L. 2013, ApJ, 765, 59
Graninger, D. M., Herbst, E., Öberg, K. I., & Vasyunin, A. I. 2014, ApJ, 787, 74
Hacar, A., Tafalla, M., & Alves, J. 2017, A&A, 606, A123
Hatchell, J., Fuller, G. A., Richer, J. S., Harries, T. J., & Ladd, E. F. 2007, A&A, 468, 1009
Hatchell, J., Richer, J. S., Fuller, G. A., et al. 2005, A&A, 440, 151
Higuchi, A. E., Sakai, N., Watanabe, Y., et al. 2018, ApJS, 236, 52
Hirota, T., Bushimata, T., Choi, Y. K., et al. 2008, PASJ, 60, 37
Hirota, T., Honma, M., Imai, H., et al. 2011a, PASJ, 63, 1
Hirota, T., Ikeda, M., & Yamamoto, S. 2001, ApJ, 547, 814
Hirota, T., Ohishi, M., & Yamamoto, S. 2009, ApJ, 699, 585
Hirota, T., Sakai, T., Sakai, N., & Yamamoto, S. 2011b, ApJ, 736, 4
Hirota, T., Yamamoto, S., Mikami, H., & Ohishi, M. 1998, ApJ, 503, 717
Howe, D. A., Millar, T. J., Schilke, P., & Walmsley, C. M. 1994, MNRAS, 267, 59
Kristensen, L. E., van Dishoeck, E. F., Bergin, E. A., et al. 2012, A&A, 542, A8
Lucas, R., & Liszt, H. 1998, A&A, 337, 246
Milam, S. N., Savage, C., Brewster, M. A., Ziurys, L. M., & Wyckoff, S. 2005, ApJ, 634, 1126
Pagani, L., Vastel, C., Hugo, E., et al. 2009, A&A, 494, 623
Pineda, J. E., Goodman, A. A., Arce, H. G., et al. 2011, ApJL, 739, L2
Prodanović, T., Steigman, G., & Fields, B. D. 2010, MNRAS, 406, 1108
Rosolowsky, E. W., Pineda, J. E., Foster, J. B., et al. 2008, ApJS, 175, 509
Sakai, N., Sakai, T., Hirota, T., Burton, M., & Yamamoto, S. 2009, ApJ, 697, 769
Sakai, N., & Yamamoto, S. 2013, ChRv, 113, 8981
Sakai, T., Sakai, N., Furuya, K., et al. 2012, ApJ, 747, 140
Sonneborn, G., Tripp, T. M., Ferlet, R., et al. 2000, ApJ, 545, 277
Suzuki, H., Yamamoto, S., Ohishi, M., et al. 1992, ApJ, 392, 551
Talbi, D., Ellinger, Y., & Herbst, E. 1996, A&A, 314, 688
Tobin, J. J., Looney, L. W., Li, Z.-Y., et al. 2016, ApJ, 818, 73
van der Tak, F. F. S., Black, J. H., Schöier, F. L., Jansen, D. J., & van Dishoeck, E. F. 2007, A&A, 468, 627
van der Tak, F. F. S., Müller, H. S. P., Harding, M. E., & Gauss, J. 2009, A&A, 507, 347
van Dishoeck, E. F., Blake, G. A., Jansen, D. J., & Groesbeck, T. D. 1995, ApJ, 447, 760
Watson, W. D. 1974, ApJ, 188, 35
Woodruff, H. C., Eberhardt, M., Driebe, T., et al. 2004, A&A, 421, 703
Yoshida, K., Sakai, N., Nishimura, Y., et al. 2018, PASJ, in press
Zapata, L. A., Arce, H. G., Brassfield, E., et al. 2014, MNRAS, 441, 3696